

## Stratified Ekman layers

James F. Price<sup>1</sup>

Department of Physical Oceanography, Woods Hole Oceanographic Institution  
Woods Hole, Massachusetts

Miles A. Sundermeyer<sup>1</sup>

Joint Program in Physical Oceanography, Massachusetts Institute of Technology  
and Woods Hole Oceanographic Institution, Woods Hole

**Abstract.** Under fair weather conditions the time-averaged, wind-driven current forms a spiral in which the current vector decays and turns clockwise with increasing depth. These spirals resemble classical Ekman spirals. They differ in that their rotation depth scale exceeds the  $e$ -folding depth of the speed by a factor of 2 to 4 and they are compressed in the downwind direction. A related property is that the time-averaged stress is evidently not parallel to the time-averaged vertical shear. We develop the hypothesis that the flat spiral structure may be a consequence of the temporal variability of stratification. Within the upper 10–20 m of the water column this variability is associated primarily with the diurnal cycle and can be treated by a time-dependent diffusion model or a mixed-layer model. The latter can be simplified to yield a closed solution that gives an explicit account of stratified spirals and reasonable hindcasts of midlatitude cases. At middle and higher latitudes the wind-driven transport is found to be trapped mainly within the upper part of the Ekman layer, the diurnal warm layer. At tropical latitudes the effects of diurnal cycling are in some ways less important, and Ekman layer currents are likely to be significant to much greater depths. In that event the lower part of the Ekman layer is likely to be affected by stratification variability that may be nonlocal.

### 1. Observing and Modeling Wind-Driven Currents

The upper ocean Ekman layer problem was defined in a complete and almost modern form in Walfrid Ekman's landmark analysis of 1905. From very limited observations, *Ekman* [1905] inferred that the momentum balance for steady wind-driven currents must be primarily between the Coriolis acceleration acting on the current and the divergence of a turbulent stress imposed by the wind. He understood that a model of wind-driven currents must be built around a model of the turbulent stress and went on to show how field observations and diffusion theory might be used to develop such models. Despite this promising beginning and a long history of research, there are fundamental aspects of the Ekman layer problem that remain unsettled, including even the list of important external variables. The great and en-

during difficulty is that turbulent stress is important at lowest order in the Ekman layer, and yet is almost impossible to measure in situ against a background of surface gravity waves. Thus the observational basis needed for a full understanding of the Ekman layer is incomplete. Measurement of Ekman layer currents presents similar challenges, but modern measurement tools and techniques [*Weller and Davis*, 1980; *Weller*, 1981] have now given what appears to be a detailed and reliable view of wind-driven currents under fair weather conditions [*Price et al.*, 1986; *Wijffels et al.*, 1994; *Chereskin*, 1995].

#### 1.1. Goals, Scope, and Outline

Our goals are to describe the vertical structure of wind-driven currents using these historical field observations and then identify the simplest models that can serve to explain and predict this structure. Toward these goals we take up four questions in turn:

**1.1.1. Question 1: What is the structure of the fair weather Ekman layer?** By structure we mean the shape and thickness of the current profile, including the current direction. This question is addressed first by a review and analysis of the field observations noted above (in section 2). The scope of this study is limited to open ocean and fair weather conditions (wind

<sup>1</sup>Now at Center for Marine Science and Technology, University of Massachusetts, New Bedford.

Copyright 1999 by the American Geophysical Union.

Paper number 1999JC900164.

0148-0227/99/1999JC900164\$09.00

stress less than  $\sim 0.2$  Pa and significant solar heating), primarily because those are the conditions that held in the present data sets. Other important cases, e.g., the winter Ekman layer [Krauss, 1993; Schudlich and Price, 1998] and the Ekman layer under ice [McPhee, 1990] are omitted from consideration, though we will try to indicate where the transition to other regimes may occur.

**1.1.2. Question 2: Does the classical diffusion theory lead to a useful model of the fair weather Ekman layer?** Ekman's [1905] classical diffusion theory was one of the first attempts to apply ideas of turbulent transfer to a natural system, and it remains valuable today as a reference or starting point for boundary layer models. The present analysis shows that a very simple, optimized classical diffusion model can give a fairly good account of the observed Ekman layer. There are small but systematic errors, however, and a more realistic model evidently requires a complex diffusion coefficient (sections 3 and 6).

**1.1.3. Question 3: What physical processes have to be represented in a minimum, realistic model of the fair weather Ekman layer?** The central hypothesis of this analysis is that time-dependent variations of stratification are crucially important for the upper ocean Ekman layer. One important mode of fair weather variability is the diurnal cycle, evidence of which is reviewed in section 4. A time-dependent diffusion model that incorporates a diurnal cycle is shown to give a qualitatively realistic Ekman layer structure (section 4). A layered model of this process can be integrated to yield an approximate, closed solution for a stratified Ekman layer (sections 5.1 and 5.2). (This solution is a successor to the Price *et al.* [1986] numerical model.) Comparison of this model with midlatitude cases is generally favorable, while comparison with a tropical case is less so, perhaps because of neglected stratification variability in the lower part of the Ekman layer (section 7).

**1.1.4. Question 4: How does the Ekman layer structure vary with wind stress, latitude, and other external variables?** The observations alone provide a very limited view of parameter dependence, and a full assessment requires a model (section 5.4). A fundamental and conventional assumption is that the Ekman layer structure is determined mainly by the local surface fluxes (wind stress and heat fluxes) and by Earth's rotation. A secondary assumption, made in the hope that simple models and explicit solutions will suffice for prediction, is that the surface fluxes can be represented well enough by suitable time averages. Neither of these is strictly true, and part of the analysis will seek to evaluate the resulting errors and suggest remedies.

Finally, our attempt to answer the questions posed above is summarized in section 8, where we also point out some of the many missing pieces to a complete understanding of the Ekman layer problem. The remainder of this section defines the terms of a familiar momentum balance.

## 1.2. An Upper Ocean Momentum Balance

This analysis is meant to treat the local response of currents, aside from all consequences of topography and spatially varying wind stress. Thus it will apply only to deep, open ocean regions away from the equator. Consideration is also limited to regimes in which the momentum balance of an observed horizontal current  $v_o$  (averaged over tens of minutes) is nearly linear and can be written in the usual form,

$$\frac{\partial v_o}{\partial t} + ifv_o = \frac{1}{\rho} \frac{\partial \tau}{\partial z} - \frac{1}{\rho} \nabla P + \text{HOT} \quad (1)$$

where  $f$  is the Coriolis parameter,  $\rho$  is the nominal density of seawater,  $\nabla P$  is the horizontal pressure gradient, and HOT are higher-order terms, for example, a horizontal eddy stress, that are presumed small. Bold symbols are complex with components (real, imaginary) = (crosswind, downwind). The stress  $\tau$  is a turbulent momentum flux,  $\tau = -\rho \langle v'_o w' \rangle$ , where angel brackets denote a time average over tens of minutes and  $w$  is the vertical component of velocity. As noted at the outset, turbulence measurements able to resolve this momentum flux are generally not possible over the open ocean, though some important qualitative features of upper ocean turbulence are known from observations and are referred to in section 4. (For contrast, see *McPhee and Martinson* [1994] for detailed turbulent stress measurements below an ice cover.) Thus the present analysis deals solely with current phenomena rather than with turbulence per se. This is a significant limitation insofar as quite different parameterizations of turbulent stress may give rather similar current profiles, and, of course, turbulence properties are important in their own right.

The important pressure gradient term could result from tides, eddies, or perhaps the basin-scale circulation but not, presumably, directly from the local wind. That being so, the observed current can be decomposed into a sum of wind- and pressure-driven components [McPhee, 1990],  $v_o = v + v_p$ , where the momentum balance of the wind-driven current is then

$$\frac{\partial v}{\partial t} + ifv = \frac{1}{\rho} \frac{\partial \tau}{\partial z}. \quad (2)$$

How this decomposition might be accomplished with field observations is reviewed in section 2.1. It is helpful to think of the wind-driven current as being the sum of a free mode, or inertial oscillation, for which the Coriolis force is balanced by the local acceleration, and a forced mode, also called the Ekman current, for which the Coriolis force is balanced by the divergence of the wind stress. Inertial oscillations are a prominent feature of most upper ocean current records and are an important element of upper ocean dynamics. Nevertheless, the forced mode, Ekman current is the main interest here since it represents the time-mean effect of direct wind forcing. To detect the Ekman current in field ob-

servations requires time averaging over a long enough interval,  $O(10)$  inertial periods or more, to suppress inertial motions so that (2) reduces to

$$\mathbf{V} = \frac{-1}{\rho f} \frac{\partial \overline{\boldsymbol{\tau}}}{\partial z} \quad (3)$$

with  $\mathbf{V} = \overline{\mathbf{v}}$  (the overline on stress is omitted hereafter). The passage from (2) to (3) appears trivial, though not for diffusion parameterizations, as we will show in section 4.

For many purposes, and especially those involving the large-scale ocean circulation, the most important property of the Ekman current is its volume transport  $\mathbf{M}$ , given by the vertical integral of (3). This requires boundary values of the stress. We are considering deep water cases so that the stress and the wind-driven current may be presumed to vanish at a depth  $z_r$  within the water column and  $O(100 \text{ m})$ . The wind-driven transport between  $z_r$  and a shallower depth  $z$  is then related to the stress at  $z$  by

$$\mathbf{M}(z) = \frac{-i}{\rho f} \boldsymbol{\tau}(z), \quad (4)$$

which shows that the transport below  $z$  and the stress at  $z$  are perpendicular. This will be referred to as the transport/stress relationship. If  $z$  is the sea surface, then the stress is the wind stress  $\boldsymbol{\tau}_w$  and the transport is the total wind-driven transport or Ekman transport. It is well known that the Ekman transport is independent of the details of turbulent transfer within the Ekman layer, though this is not true for the transport at any other depth. The Ekman transport relation is thus plausible a priori, and it has also been verified in a variety of direct and indirect ways [Chereskin, 1995; Weller and Plueddemann, 1996]. In this analysis it will be assumed that the observed, total wind-driven transport should satisfy the Ekman transport relationship to within measurement and sampling errors. The transport relationship is then available as a consistency check on the estimated current (section 2.2). Notice that the only consequence of the wind is presumed to be the stress, and all effects of surface gravity waves, e.g., enhanced turbulent mixing near the surface [Anis and Moum, 1995] and Stokes drift [McWilliams et al., 1997] have been neglected for simplicity.

For some other purposes, e.g., hindcasting the wind-driven currents in surface drifter or ship drift data [Krauss, 1996; Niiler and Paduan, 1995], it may be necessary to calculate the profile of the time-averaged current  $\mathbf{V}(z)$ . This requires a solution to the Ekman layer problem that can be evaluated using readily available wind stress, etc., from a climatology and is a goal of this analysis.

## 2. Historical Field Observations of the Upper Ocean Ekman Layer

Accurate and detailed field observations provide essential guidance in the development of Ekman layer models. The most useful data sets are those including current measurements that resolve the full profile of the Ekman layer current, along with direct wind measurements sufficient to estimate the wind stress.

### 2.1. Data Sets and Their Analysis

Two examples of such data sets are the third setting of the Long-Term Upper Ocean Study (LOTUS3) [Briscoe and Weller, 1984; Price et al., 1987] and the Eastern Boundary Current (EBC) observations described by Chereskin [1995]. Both data sets were acquired from surface moorings deployed for at least 4 months and included good near-surface, vertical resolution of currents and measurements of wind velocity. There were some significant differences in the sampling and measurement methods that will affect how these data can be used in the analysis of sections 3 and 4: the LOTUS3 mooring measured currents with vector-measuring current meters that also measured temperature and thus gave a useful estimate of stratification; the EBC mooring employed a single Doppler acoustic current meter that gave very good and consistent depth resolution of currents within the upper ocean, though without temperature measurement.

The LOTUS3 data were collected over the summer at 35°N in the western Sargasso Sea. Fair weather prevailed during most of this period; the average wind stress amplitude was  $\tau_w = 0.07 \text{ Pa}$ , and the average of the daily maximum net surface heat flux was  $Q = 630 \text{ W m}^{-2}$  (Table 1 and see Price et al. [1987] for details of the analysis). The EBC mooring data reported by Chereskin [1995] was taken at 37°N in the eastern North Pacific and also during the summer. The average wind stress was  $\tau_w = 0.09 \text{ Pa}$  over the period analyzed. The heat flux was not reported by Chereskin [1995] and has been estimated from solar radiation climatology [Peixoto and Oort, 1992] to be  $Q \approx 570 \text{ W m}^{-2}$  or  $\sim 10\%$  less than at LOTUS3 because of slightly heavier cloud cover. (Sensitivity of some model solutions to errors in the surface fluxes are evaluated in section 5.4.1.) Overall, the external conditions were very similar at LOTUS3 and EBC.

A third interesting data set was reported by Wijffels et al. [1994], who made acoustic doppler current profiles, conductivity-temperature-depth (CTD) profiles, and wind measurements across the North Pacific at 10°N latitude. They divided their analysis of the Ekman layer into three segments that differed mainly with respect to the depth of the top of the main thermocline and the reference depth (deeper in the west). Here the western and central segments have been averaged to produce a single profile. The wind stress was  $\tau_w =$

**Table 1.** External Variables and Estimated Transport and Current Profile Scales.

Data Set	$Q$ , $W\ m^{-2}$	$f$ , $10^{-5}\ s^{-1}$	$\tau_w$ , Pa	$M_w$ , $m^2\ s^{-1}$	$M_o$ , $m^2\ s^{-1}$	$L_s$ , m	$L_\theta$ , m
LOTUS3	630	8.36	0.07	0.81	(0.76, -0.02)	10	18
EBC	570	8.77	0.09	1.00	(1.02, 0.08)	16	66
10°N	560	2.53	0.11	4.23	(3.05, 0.12)	32	150

$Q$  is the average of the daily maximum surface heat flux,  $f$  is the Coriolis parameter,  $\tau_w$  is the magnitude of time-averaged wind stress,  $M_w$  is the expected Ekman transport (all in the crosswind direction),  $M_o$  is the observed transport (crosswind, downwind),  $L_s$  is the  $e$ -folding depth scale of the current speed estimated by fitting an exponential to the current profile, and  $L_\theta$  is the depth over which the current turns through 1 rad, estimated by fitting a straight line to the direction profile. LOTUS3 is the Long-Term Upper Ocean Study, while EBC refers to Eastern Boundary Current.

0.11 Pa or a little larger than the other two cases, and the heat flux estimated from climatology was also about the same. A significant difference from the previous subtropical cases is that the Coriolis parameter was smaller by more than a factor of 3, and thus the expected Ekman transport is larger by a similar factor (Table 1).

The observed upper ocean current includes significant contributions from internal and external tides and quasi-geostrophic eddies that are not directly wind driven. In order to separate the wind-driven current from these other, mainly pressure-driven currents, there has to be an analysis procedure based upon some preconception of the wind-driven and pressure-driven current. The assumption made in the LOTUS3 and EBC analysis was that Ekman layer currents are more strongly surface trapped than are other, mainly pressure-driven currents [Price *et al.*, 1987; Davis *et al.*, 1981a]. The latter could thus be estimated as the observed current at a reference depth  $z_r$  chosen to be below the greatest expected depth of the Ekman layer (and thus the preconception). The observed current at the reference level was then subtracted from the observed upper ocean current  $v_o(z)$  to leave an estimate of the wind-driven current above  $z_r$ ,

$$v(z) = v_o(z) - v_o(z_r).$$

In the LOTUS3 analysis the reference depth was  $z_r = 50$  m, somewhat below the depth of the surface mixed layer (typically 5 to 30 m thick in the LOTUS3 data set, parts of which are examined in section 4). Thus the water column above the reference depth and including the Ekman layer was stably stratified on time average. A similar reference depth was used in the EBC analysis. (Momentum and energy supplied to the surface layer by the wind could be transported vertically to much greater depths by propagating waves or Ekman pumping [Lee and Eriksen, 1996]. This kind of process is inherently nonlocal but could lead to deep currents that are coherent with the local wind and thereby confound this attempt at separation. It is clear that we are excluding this kind of process from our definition of Ekman currents, (3), but, of course, we cannot exclude it from the field experiments.)

There is a danger of circularity associated with this analysis procedure since we expected a surface-trapped Ekman layer, and that is what was found (Figure 1). However, the estimated Ekman layer thickness measured by the speed  $e$ -folding (Table 1) was considerably less than the reference depth, and thus the analysis allowed for the possibility of a much thicker Ekman layer. As well, in the LOTUS3 case the vertical shear of the total current was comparatively small at the reference depth, so that the resulting Ekman layer currents (and certainly the  $e$ -folding and the turning depth) were not extremely sensitive to the reference depth. This is less true for the 10°N case and generally for the transport (see Chereskin [1995] for more detail of the EBC case and Schudlich and Price [1998] for more on LOTUS3). In the end there is no guarantee that this simple analysis procedure has managed to exclude all of the pressure-driven current, including especially the thermal wind, while retaining all of the wind-driven current. A skeptic might prefer to regard the resulting upper ocean currents as the shear over a fixed depth interval, though for economy of language we will describe them as if they were absolute, wind-driven currents.

## 2.2. Uncertainties in the Estimated Ekman Current

The most difficult (and unsatisfactory) part of this analysis is to make a meaningful estimate of the uncertainty in the estimated wind-driven currents. Statistical error estimates were reported for the time-averaged current (LOTUS3 and EBC) or the transport (10°N). Standard errors were roughly 15 to 20% of the mean. Statistical uncertainties are useful but not conclusive for the present purpose since the time-averaged current could be statistically stable and yet not be wind driven as intended here.

It is also useful to know how well the estimated transport follows the Ekman transport relation. In both subtropical cases the transport relation was satisfied to within  $\sim 10\%$ , which is within the uncertainty in the estimated wind stress, usually estimated at  $\sim 20\%$  [Large and Pond, 1981]. In the 10°N case the transport discrepancy was considerably larger,  $\sim 30\%$ , in the sense

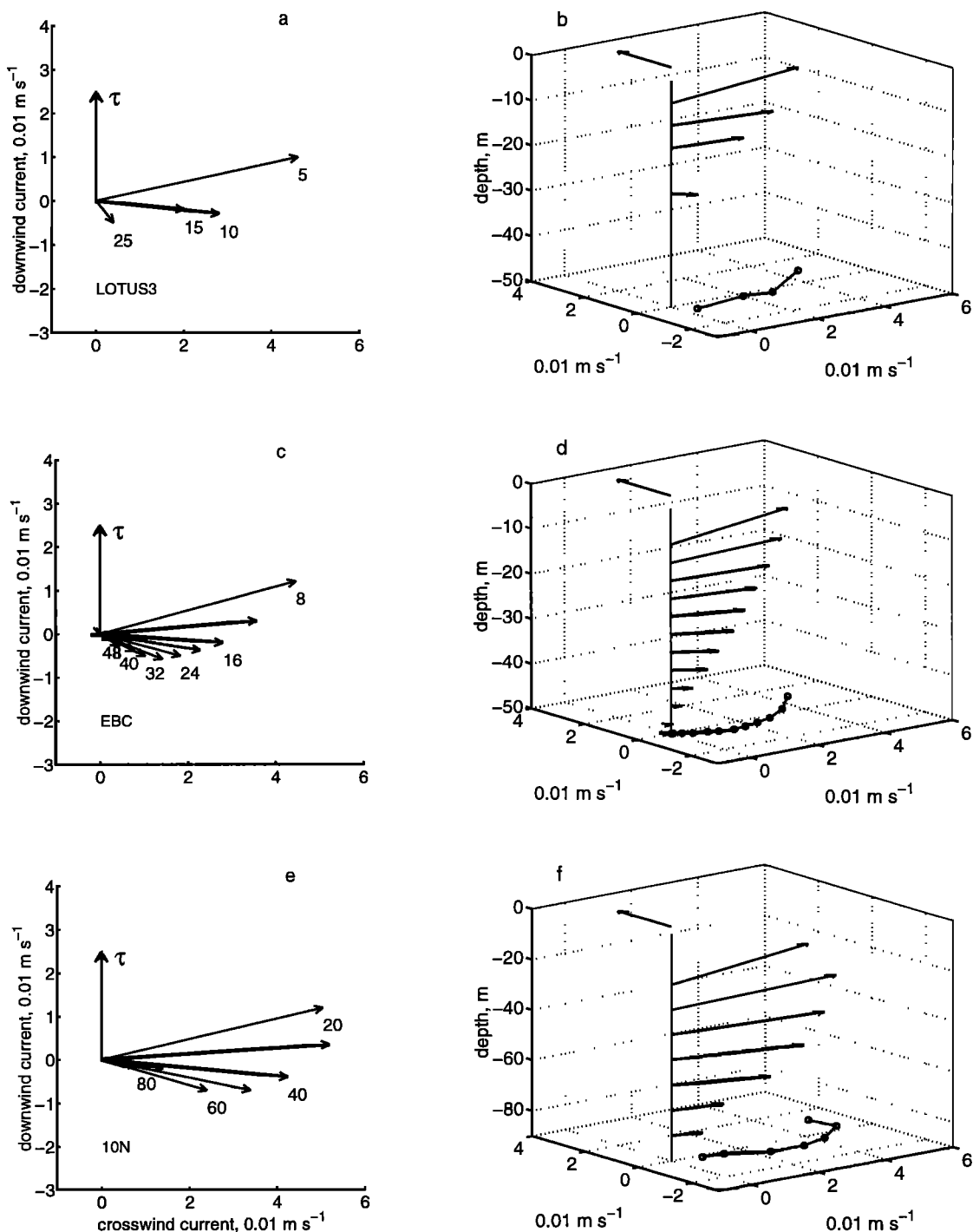


**Figure 1.** Hodographs and three-dimensional profiles of time-averaged upper ocean currents and wind stress. (a, b) Observations from the Long-Term Upper Ocean Study (LOTUS3) in the western Sargasso Sea [after *Price et al.*, 1987]. (c, d) Observations from the Eastern Boundary Current Experiment [after *Chereskin*, 1995]. (e, f) Observations from 10°N in the Pacific [after *Wijffels et al.*, 1994]. The depth in meters is just below the tip of the hodograph vectors. The reference frames have been rotated so that the wind stress points due “north” (the  $\tau$  vector indicates direction only). Notice that the vertical resolution and the number of observation depths varied from case to case and that the shallowest observations were some distance below the surface, 5, 8 and 20 m, respectively. Note, too, the change in depth scale going from Figures 1b and 1d to Figure 1f.

that the observed transport was less than the expected Ekman transport [Wijffels *et al.*, 1994]. Whether this discrepancy was due to sampling or measurement error (the record was comparatively short in duration and did not sample the upper 20 m) or due to the HOT of (1) is not known. Despite this comparatively large uncertainty the 10°N data set is very valuable for this analysis since it provides at least a glimpse of parameter space.

If the transport uncertainty or discrepancy (whichever is larger) was due to a current error distributed uniformly over the interval  $0 > z > z_r$ , then the current error would be roughly  $0.004 \text{ m s}^{-1}$  in the two subtropical cases and  $\sim 0.012 \text{ m s}^{-1}$  in the 10°N case. This sets a lower bound on the root-mean-square error that a model will make when simulating these data sets, since all of the model solutions satisfy the Ekman transport relation exactly and errors, whether measured or modeled, are likely to be depth dependent.

### 2.3. Structure of the Ekman Layer

It is most encouraging that the analyzed Ekman layer currents were quite similar in the two subtropical cases (Figure 1) despite very different measurement and averaging methods. In all three cases the Ekman layer currents form a spiral-shaped profile in which the current vector decays and rotates clockwise with increasing depth. The shallowest measured currents were about  $0.05 \text{ m s}^{-1}$  and about  $75^\circ$  to the right of the wind. The spirals differ mainly in their thickness; in the subtropical cases the  $e$ -folding depth of the current speed  $L_s$  was  $\sim 10$  to  $15 \text{ m}$ , while in the tropical case  $L_s \approx 30 \text{ m}$ . (Figure 2). Thus the larger Ekman transport at lower latitudes appears to be taken up by a thicker Ekman layer rather than by an increased current speed (this likely depends upon the depth of semipermanent stratification, discussed more in section 7).

The observed spirals, dubbed “stratified Ekman spirals” [Price *et al.*, 1987] for reasons developed further in sections 4 and 5, have a shape that is somewhat similar to that of a classical Ekman spiral. A difference in detail

is that compared to a classical Ekman spiral; the speed of the current decreases with depth more rapidly than the current vector rotates to the right (noted also by Chereskin [1995], Price *et al.* [1986], and Schudlich and Price [1998]), and these spirals appear to be flattened or compressed in the downwind direction. In effect, the direction and speed vary on different depth scales, with the former being larger. The shape of the spiral can be quantified by a “flatness”  $F_l$ , the ratio of amplitude decay to the turning rate,

$$F_l = \frac{\partial S}{\partial z} \left( S \frac{\partial \theta}{\partial z} \right)^{-1},$$

where  $S$  is the speed of the current. In a classical Ekman spiral (infinite water depth, section 3.1) the speed decreases by one  $e$ -folding over a depth interval within which the current turns through 1 rad and  $F_l = 1$ . The spirals of Figure 1 have an overall flatness,  $F_l = L_\theta/L_s \approx 2 - 3$ , based upon the ratio of the turning depth to the  $e$ -folding depth. When estimated by finite differences over the discrete data,  $F_l \approx 2$  averaged over the upper half of the Ekman layer and  $F_l \approx 3$  over the lower half. An alternate and in some ways more robust way to quantify the spiral shape is by the ratio of the standard deviations of the crosswind and downwind current components,

$$F_v = \frac{\text{rms}U'}{\text{rms}V'},$$

where prime indicates the departure from the depth mean.  $F_v$  is also  $\sim 2-3$  in these cases.

The task for Ekman layer models can now be stated all too succinctly: to account for the  $e$ -folding scale of the Ekman layer (i.e., the speed  $e$ -folding) as well as the flat spiral shape or, equivalently, the length scales for both speed and direction.

### 3. Diffusion Theories

The classical theory of wind-driven currents was developed by Ekman [1905] on the important new understanding that a model of wind-driven currents must ac-

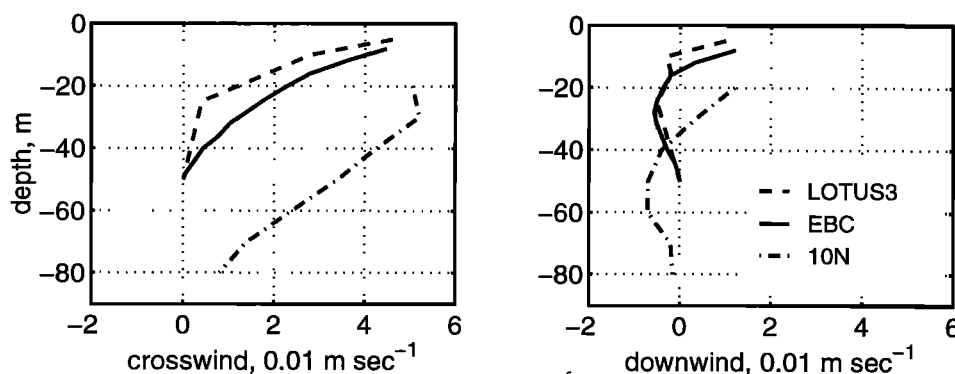


Figure 2. (left) Crosswind and (right) downwind current components on a common depth scale. Note the much thicker Ekman layer observed along 10°N.

count for the turbulent transfer of momentum downward from the sea surface. Modeling turbulent transfer presents a challenge in the simplest circumstance, especially so in the upper ocean, where gravity waves and variable wind stress and heat flux are the rule. As a first model of turbulent transfer Ekman adopted Boussinesq's eddy diffusion parameterization of circa 1877,

$$\tau/\rho = K \frac{\partial v}{\partial z}, \quad (5)$$

where  $K$  is the eddy diffusivity (a concise and sympathetic review of the eddy diffusivity parameterization is given by *Frisch* [1995]; also see *Brown* [1991]). A physical interpretation of  $K$  is that it represents the stirring effects of turbulence; stirring the vertical shear of a current produces a momentum flux down the local gradient. Similar turbulent transfer parameterizations are widely used in ocean modeling, though are seldom the central issue, as is the case here.

The use of this parameterization shifts the Ekman layer problem onto the task of finding the appropriate  $K$ . *Ekman* [1905] knew from observations that the surface current was of the order of a few percent of the wind speed, which implies a boundary layer thickness of a few tens of meters and  $K$  that is  $O(100 \times 10^{-4}) \text{ m}^2 \text{ s}^{-1}$ ; but he also suspected that  $K$  would have a lively dependence upon external and internal parameters, wind speed and stratification, at least. Considerable effort has gone toward estimating  $K$  from field observations [*Rosby and Montgomery*, 1935; *Neumann and Pierson*, 1966; *Pollard*, 1975; *Huang*, 1979; *Schudlich and Price*, 1998], though it is not evident that an accepted form of the upper ocean  $K$  has emerged from this "inductive diagnostic" program.

Our expectation is that there should exist a systematic stress/shear relationship, this being different only in detail from our assumption (question 4, section 1.1.4) that the current profile holds a systematic relationship to the external variables. It remains to be seen whether the upper ocean stress/shear relationship is consistent with a physical diffusivity, i.e., a  $K$  that could be related to measurable, physical turbulence properties or to a formal diffusivity, i.e., any consistent relationship between stress and shear. To arrive at estimates of  $K$ , we will first compare the observations to simple solutions, much the way Ekman suggested, and then estimate  $K$  using the steady momentum balance and the data alone. By this roundabout path we hope to gain some insight into the difficulties encountered by the inductive diagnostic program and will finally conclude that the fair weather, upper ocean  $K$  is formal rather than physical.

### 3.1. Laminar Diffusion Model

If the diffusivity is presumed to be steady but possibly dependent upon external variables and depth, then from (3) and (5) the momentum balance for the time-averaged current is just,

$$ifV = \frac{\partial}{\partial z} K \frac{\partial V}{\partial z} \quad (6)$$

and the associated model is termed a "classical" diffusion model. Thus a classical model attempts to calculate the mean current (and the mean stress) directly. If, in addition,  $K$  is presumed to be constant with depth, then the model will be termed a classical "laminar" diffusion model or CLDM. (Nonclassical varieties have also been proposed. Section 4 considers briefly a model with depth and time varying diffusivity.  $K$  could be flow dependent and thus implicitly depth and time dependent as in  $K$  theory models, for example, by *Mellor and Durbin* [1975], or the bulk boundary layer model of *Large et al.* [1994]. These latter models encompass the dynamics investigated in sections 4 and 5. Nonclassical diffusion models generally have to be solved numerically and, for that reason, are not emphasized here.) The CLDM has as a solution the classical Ekman spiral, which is a valuable reference or touchstone for boundary layer observations and theories [e.g., *Stacey et al.*, 1986]. The simple CLDM is unlikely to be the best possible diffusion model, but before going on to more complex models, it is useful to identify clearly what its shortcomings may be.

In all of the solutions considered here the wind stress is taken to be steady and northward (or imaginary) and the surface boundary condition at  $z = 0$  is

$$K \frac{\partial V}{\partial z} \Big|_{z=0} = i\tau_w/\rho,$$

where  $\tau_w$  is the given wind stress. The lower boundary condition is that the stress (and thus the current shear) vanish at the given depth  $H$ ,

$$\frac{\partial V}{\partial z} \Big|_{z=-H} = 0.$$

In section 7 we will consider how time variations of  $H$  may affect the Ekman layer, but for now,  $H$  is taken to be the constant reference depth  $z_r$ , when simulating the three cases of section 2. More generally,  $H$  is identified as the depth of semipermanent stratification, i.e., the top of the seasonal or main thermocline (as mapped by *Levitus* [1982], for example). Subject to these boundary conditions, the solution for the wind-driven current is

$$V = U_H \alpha \frac{r}{1-s} [\exp(r\alpha z') + s \exp(-r\alpha z')] \quad (7)$$

over the depth range  $z' = z/H > -1$  and zero below. The scale

$$U_H = \frac{U_*^2}{Hf}$$

is called the "neutral" velocity scale, where  $U_* = \sqrt{\tau_w/\rho}$  is the friction velocity. If the Ekman transport were evenly distributed over the depth  $H$ , then the surface current would have a speed  $U_H$ . Any process that causes the Ekman transport to be surface trapped will

increase the surface speed above  $U_H$ . The degree of surface trapping is defined by

$$\alpha = H/D_K$$

where

$$D_K = \sqrt{2K/f} \quad (8)$$

is the diffusive (Ekman) depth scale. The coefficients are  $r = \sqrt{2}\exp(i\pi/4)$  and  $s = \exp(-2r\alpha)$ .

This solution simplifies in two limits: If the diffusive depth scale is comparable to or greater than  $H$ , then  $\alpha < 1$  and the solution approaches the strong diffusion limit,

$$\mathbf{V} = U_H[1 + i\alpha^2(z'^2 + 2z' + 2/3)] \quad (9)$$

found by expansion to fourth order in  $\alpha$ . In this limit the Ekman layer current is almost depth independent with amplitude  $U_H$  and is almost at a right angle to the wind stress (Figure 3a). There is significant vertical shear in the downwind direction, and it is instructive to consider why the current profile has this particular form. In the strong diffusion limit the transport increases almost linearly with depth above  $z = -H$  as  $M(z) = (H + z)U_H$ . The current profile satisfies the transport/stress relationship (4), and thus the stress also increases linearly with depth as  $\tau(z) = i\rho fM(z)$ . If  $K$  is constant, then the vertical shear in the downwind current must also increase linearly with depth and the downwind current thus has quadratic depth dependence (Figure 4). (It is easy to generalize this to other forms of  $K(z)$ , and, for example, a  $K$  that decreases linearly with depth as  $1 + z'$  gives a linear current profile that is little different from that obtained with constant  $K$ .) In this small- $\alpha$  profile the current turns with depth more rapidly than it decays and  $F_l \leq 1$  throughout the Ekman layer. (The profile shape in this model is determined by  $\alpha$  and by the boundary condition at  $z = -H$ . A no-slip condition, which would be more appropriate for the seafloor, gives profiles having  $F_l \geq 1$  owing to compression or flattening in the crosswind direction. In the limit of very large mixing ( $\alpha \ll 1$ ) the no-slip solution approaches plane Couette flow,  $U(z) = i(1 - z')U_*^2/K$  having linear shear in the downwind direction.) Note that there is a large and unphysical discontinuity of the current across the base of the Ekman layer at  $z' = -1$ , a first hint that the lower boundary condition will require further thought. As  $\alpha$  vanishes, the Ekman layer current becomes sensibly uniform with depth, approaching

$$\mathbf{V} = U_H \quad (10)$$

(real component only), also termed the null model.

In the weak diffusion limit that  $\alpha \gg 1$  this solution reduces to the classical Ekman spiral for infinite water depth,

$$\mathbf{V} = U_H\alpha(1 + i)\exp(\alpha z')\exp(i\alpha z') \quad (11)$$

(Figure 3b). In this limit,  $L_s = L_\theta = \alpha H$ , and thus  $F_l = 1$  throughout the Ekman layer. Though not readily apparent, this profile also satisfies exactly the transport/stress relationship and the CLDM-appropriate stress/shear relationship. The surface current is a well-known result,

$$\mathbf{V} = \frac{U_*^2}{\sqrt{fK}}\exp(i\frac{\pi}{4}), \quad (12)$$

useful for comparison to later models.

### 3.2. Evaluating the Classical, Laminar Diffusivity

The diffusivity must be evaluated to complete the solution. Rather than sift through the many forms that have been suggested [Huang, 1979], we set out to find the best fit diffusion coefficient  $K_b$  that minimizes the mean square vector misfit between the solution (7) and the observed currents,  $\epsilon = 1/N\Sigma(\mathbf{V} - \mathbf{V}_o)^2$ , case by case (Table 2) and where  $N$  is the number of points observed. This is one implementation of the inductive diagnostic program referred to above. Another method, suitable for the midlatitude cases and leading to the same result, would be to simply equate the depth scales  $L_s$  and  $L_\theta$  with the diffusive depth scale  $D_K$ .

For the subtropical cases there was a distinct minimum of the misfit and thus a well-defined  $K_b$  and a CLDM solution that looks good (Figures 5a and 5b, left). In the EBC case the CLDM solution has an rms misfit of only  $\sqrt{\epsilon} = 0.007 \text{ m s}^{-1}$ , and the percent variance (PV) is accounted for,  $\text{PV} = 100(1 - \epsilon/(1/N\Sigma V_o^2)) = 89\%$ . This rms misfit is larger than but comparable to the lower bound on the expected error estimated in section 2.2 ( $\approx 0.004 \text{ m s}^{-1}$ .) Notice that the null model accounts for a significant fraction of the variance. Since we are taking the Ekman transport relation for granted, it may be more appropriate to compute the rms misfit for the depth-dependent part of the current, in which case the PV is considerably lower (the values in parentheses in Table 2).

The  $10^\circ\text{N}$  case proved less amenable to this and to other models that will follow. The misfit did not have a sharp minimum value, and the variance accounted by the optimum solution was only 53% (or only 14% for the depth-dependent current). There are obvious, large errors, especially in the lower half of the Ekman layer (Figure 5c, left). (The poor fit of the CLDM in the  $10^\circ\text{N}$  case can be attributed, in part, to the transport discrepancy noted in section 2.2. If the wind stress is reduced by 30% to give a model-predicted transport consistent with the observed transport, then the best fit solution ( $K_b = 400 \text{ m}^2 \text{ s}^{-1}$ ) has much better statistics; the rms misfit is  $0.015 \text{ m s}^{-1}$  and  $\text{PV} = 83\%$ . The current jump across  $z = -H$  is still unrealistic; this is likely to be a shortcoming of the lower boundary condition and is not specific to the diffusion parameterization.) About



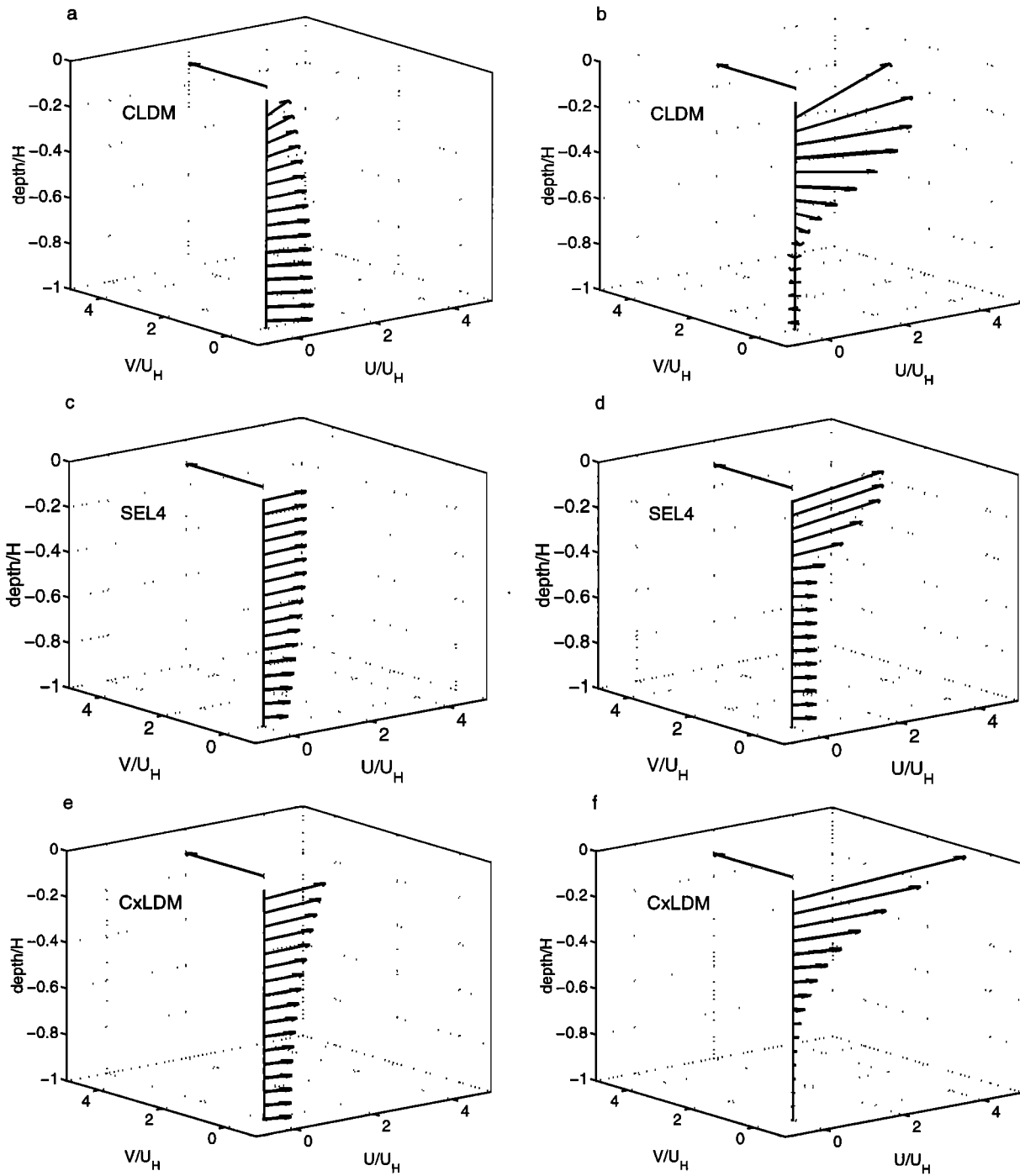


**Figure 3.** Ekman layer current profiles computed by three different models for midlatitude conditions, latitude = 37°,  $\tau_w = 0.08 \text{ Pa}$ , and  $H = 50 \text{ m}$ , which give a neutral velocity scale  $U_H = 0.022 \text{ m s}^{-1}$ , (a, b) from the Classical Laminar Diffusion Model (CLDM); (c, d) from the four-layer stratified Ekman layer model (SEL4) developed in section 5; (e, f) from the complex laminar diffusion model (CxLDM) developed in section 6. The CLDM solutions had  $K = 750 \times 10^{-4}$  and  $50 \times 10^{-4} \text{ m}^2 \text{ s}^{-1}$ , which correspond to  $\alpha = 1.2$  and 4.6 (Figures 3a and 3b, respectively). The SEL4 and CxLDM solutions had the same wind stress and  $Q = 100$  and  $1200 \text{ W m}^{-2}$  (Figures 3c and 3d and 3e and 3f, respectively), so that  $\alpha$  corresponds to the CLDM solutions at the top.

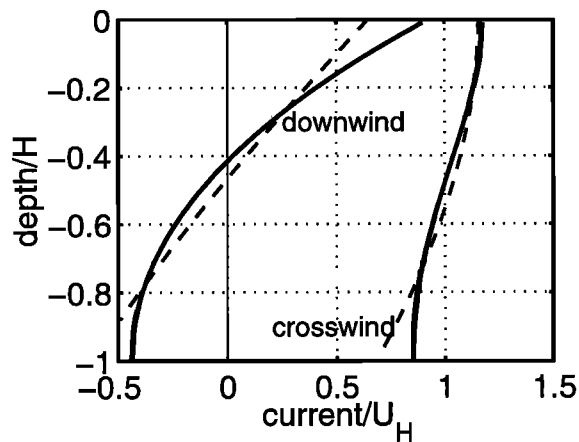


**Figure 4.** Ekman layer current components computed by the CLDM (solid line) in the small- $\alpha$  limit (parameters as in Figure 3a). The downwind current component of CLDM has a quadratic depth dependence. Also shown for comparison are solutions from a model having a diffusivity that decreases linearly with depth (dashed lines). The depth-averaged diffusivity is the same as in the CLDM. The downwind current component is then linear with depth. The crosswind current component is roughly depth independent either way.

all that can be said is that  $K_b$  appears to be larger than in the subtropical cases by a factor of  $\sim 2$  to 3.

The variation of  $K_b$  and  $L_s$  between subtropics and tropics is very roughly proportional to  $1/f$ . This is reminiscent of the parameter dependence found in steady, neutral, turbulent Ekman layers in which the only relevant time and velocity scales are  $f$  and  $U_*$  (and assuming that  $H$  is not important). That being the case, the thickness of the Ekman layer should go as  $L_s = c_1 U_*/f$ , where the similarity constant  $c_1 = 0.25 - 0.4$  [Coleman *et al.*, 1990], and diffusivity  $K = c_2 U_*^2/f$ , where  $c_2 \approx c_1^2/2 = 0.03 - 0.08$ . The estimated  $L_s$  and  $K_b$  in these cases are consistent with this  $f$ ,  $H$  dependence, though with similarity “constants”  $(c_1, c_2) \approx (0.1, 0.01)$  that are roughly a factor of 2 to 4 lower than the non-

inal, neutral values. Thus a “parameterized” CLDM having  $K = c_2 U_*^2/f$  and  $c_2 = 0.01$  gives a reasonable simulation of these cases. A simpler, more concise model is difficult to imagine.

There is trouble in the details, however. The reduced (compared to neutral) value of the similarity constant  $c_2$  suggests that some process has caused these Ekman layers to be somewhat surface trapped (stratification is considered in sections 4 and 5). It can be expected that  $c_2$  will take on other values in other circumstances, and so it is not clear that this model is useful for prediction. A close comparison of the modeled and observed spirals reveals what appears to be a consistent error in the current direction. In the EBC case the modeled currents are to the right of the observed currents by roughly  $45^\circ$  in the lower half of the Ekman layer (compare Figures 5b, left, with 5b, middle). The directional error is reduced at shallower depths and hence is equivalent to an error in flatness; the observations show  $F_l \approx 2$  near the surface and increasing somewhat with depth, while the CLDM spirals have a flatness  $F_l = 1$  near the surface and decreasing slightly with depth. To be sure, the directional or flatness error made by the CLDM is small and near the uncertainty on the observations. This error would not be considered significant for most practical purposes, but it is significant for Ekman layer modeling if, as we conclude below, it is evidence of an irreducible error in the CLDM.

### 3.3. Nonlaminar and Nonclassical Diffusivities

In an attempt to reduce the flatness error, we considered depth-dependent diffusivities. It is well known that a  $K(z)$  that increases away from a no-slip boundary can reproduce a log layer [Madsen, 1977], and we had expected to find something equivalent for the flatness. Despite a number of tries we did not discover a depth-dependent diffusivity that improved appreciably on the laminar model; solutions continued to have excessively large downwind currents, too large and positive near the surface and too large and negative at depth, and thus

**Table 2.** Statistical Measures of the Null Model and the Classical Laminar Diffusion Model (CLDM), Stratified Ekman Layer 4, and  $C_X$ LDM Solutions

Observations		Null Model		CLDM			SEL4		$C_X$ LDM	
Case	rms $V$ , $m s^{-1}$	Error, $m s^{-1}$	PV, %	$K_b$ , $10^{-4} m^2 s^{-1}$	Misfit, $m s^{-1}$	PV, %	Error, $m s^{-1}$	PV, %	Error, $m s^{-1}$	PV, %
LOTUS3	0.026	0.017	55	$100 \pm 20$	0.011	83 (58)	0.008	90 (77)	0.004	98 (94)
EBC	0.021	0.015	49	$175 \pm 25$	0.007	89 (78)	0.005	94 (89)	0.005	94 (89)
$10^\circ N$	0.036	0.027	45	$500 \pm 150$	0.025	53 (14)	0.019	73 (50)	0.016	80 (50)

SEL4 is defined in section 5, and  $C_X$ LDM is discussed in section 6. The best fit diffusivities  $K_b$ , the rms vector misfit (misfit), and the percent variance accounted for (PV) are listed for the CLDM. The rms vector error (error) is listed for the other models; this is the same statistic as misfit, but no fitting or adjustment was performed. The PV values in parentheses are for the depth-dependent part of the current.

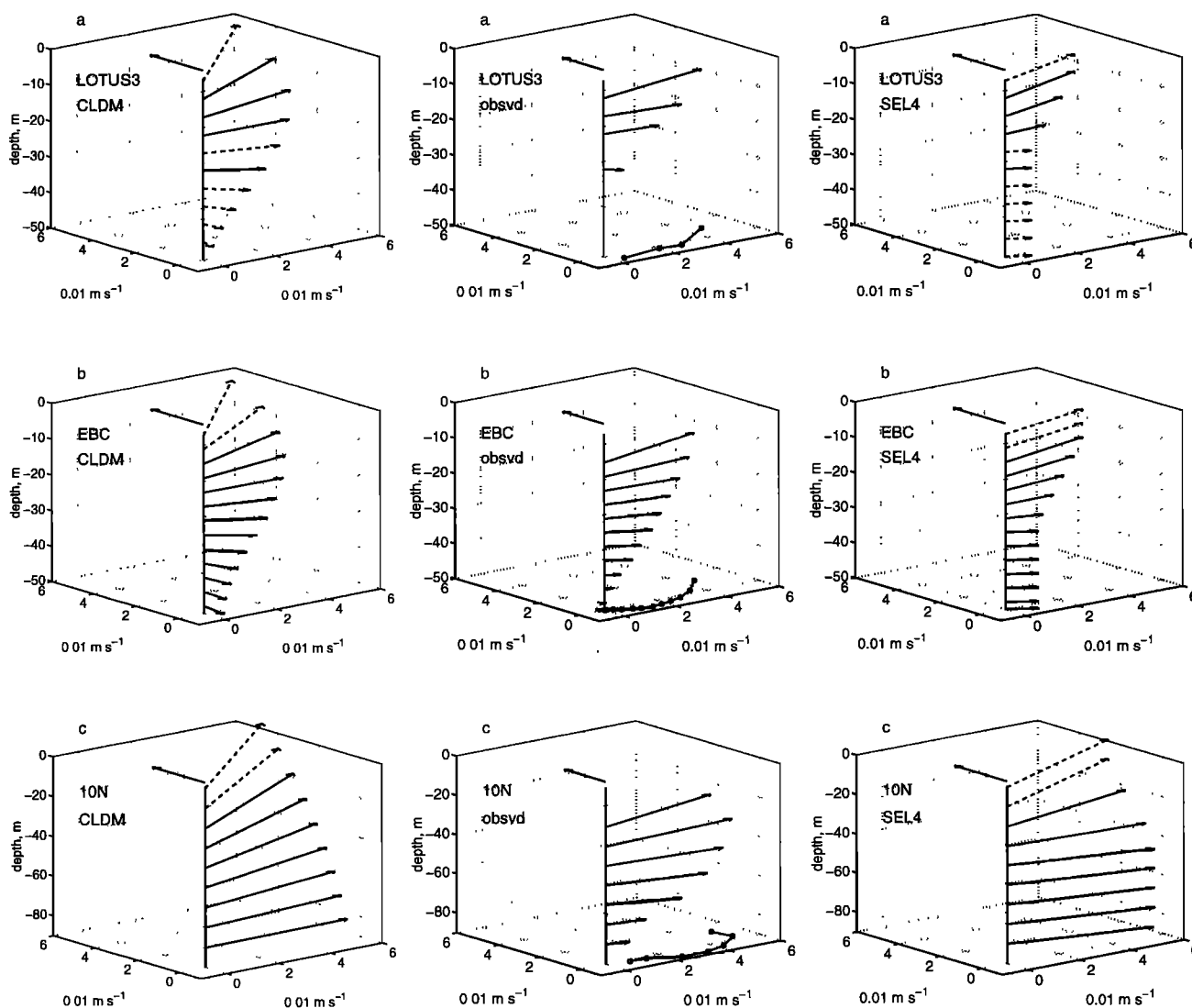


**Figure 5.** Three-dimensional profiles of the Ekman layer current computed by the (left) best fit CLDM solution, (middle) as observed (repeating part of Figure 1), and (right) as computed from the SEL4 solution developed in section 5 for (a) LOTUS 3, (b) EBC, and (c) 10°N. The model solutions are evaluated at the nominal vertical resolution of the corresponding measurements; solid (dashed) vectors correspond to depths where measurements are (are not) available.

the computed spirals did not have the flatness of the observed spirals. It appears that the classical diffusion model is unable to account for the observed, flattened spirals.

The forward problem has many possible solutions if  $K$  is regarded as poorly constrained, and so it is useful to try to diagnose the diffusivity from estimated stress and shear without involving a solution (see *Yu and O'Brien* [1991] for a different approach to this). The EBC and 10°N data are best suited for this analysis since they have good vertical resolution. The stress was not measured directly but can be inferred from the transport/stress relationship (4) by integrating the currents upward from the reference depth  $z_r$  (Figure 6 and see also *Chereskin* [1995]). In the EBC case the resulting stress profile extrapolates to approximately the

wind-derived estimate of stress at the sea surface, consistent with *Chereskin's* [1995] analysis. The vertical shear is readily computed, and the estimated stress and shear may then be compared in hodographs (Figures 6a and 6b).

The estimated stress and shear are not parallel. The stress vector points more nearly downwind than does the shear vector by as much as 40 to 50°, but depending upon depth. This nonparallel stress/shear relationship is consistent with the flatness of the observed spirals [imagine a spiral with flatness going to infinity (no downwind current component), in which case it is easy to see that the stress would have to be perpendicular to the shear at every depth] and also with the difficulty we encountered when simulating the observed current profiles with the classical diffusion model. A nonparal-

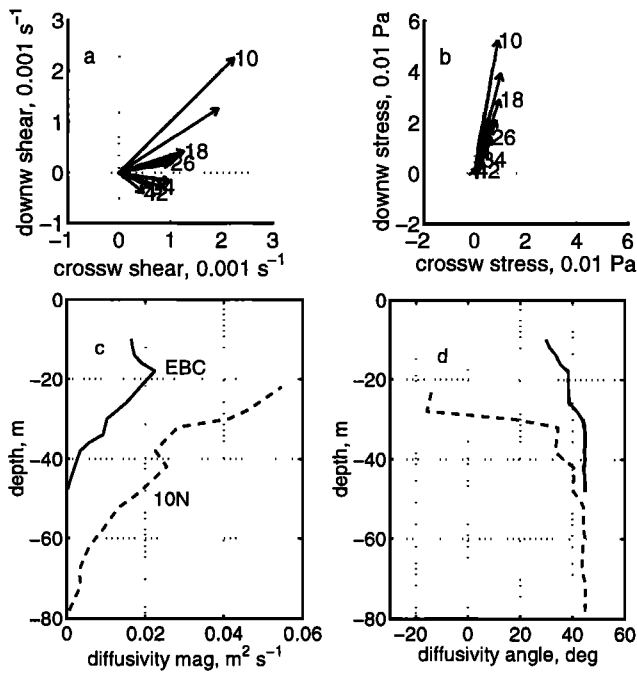


**Figure 6.** Estimated stress, shear, and diffusivity. (a) Vertical shear estimated from the EBC data set and plotted in hodograph form. Depth in meters is at the tip of every second shear vector. (b) Stress inferred from the EBC data set using the steady momentum balance. (c) Magnitude of the complex diffusivity estimated from the EBC and 10°N data sets (solid and dashed lines, respectively). (d) Rotation of the complex diffusivity, which shows the angle of the stress relative to the vertical shear. Angles greater than zero indicate that the stress vector is to the left of the corresponding shear vector, as can be seen comparing Figures 6a and 6b.

lel stress/shear relationship has also been inferred from eddy-resolving numerical model solutions of unsteady shear flows [Karniadakis and Brown, 1995] and of the planetary boundary layer [Coleman et al., 1990], where it evidently results from the nonlocal character of turbulent transfer and also from surface drifter observations [Krauss, 1993]. Whatever the source may be, a non-parallel stress/shear relationship does not appear to be consistent with a physical diffusivity or at least not with the appealing notion of local eddy stirring of the mean shear.

A complex-valued diffusivity  $K(z)$  (or a matrix diffusivity) seems to be required by this stress/shear relationship and can be readily estimated from any given data set (the EBC and 10°N versions are in Figures 6c and 6d; the LOTUS3 result is qualitatively similar to the EBC result but poorly resolved in depth). The estimated  $K(z)$  appears to have a systematic structure, and note that the phase of  $K$  indicates that stress is rotated  $\sim 45^\circ$  to the left of the shear (depth average), as expected from Figures 4a and 4b. While a complex diffusivity can be estimated, the result is not familiar,

and indeed, this  $K(z)$  is as complicated as is the current profile itself. It is fair to ask whether such a result could have either scientific or practical utility: to use this diffusivity as an explanation for the structure of the Ekman layer would require a convincing explanation of the amplitude and rotation of  $K$ ; to use this diffusivity for prediction would require an understanding of how  $K$  varied with external parameters. These new tasks are no advance on the original Ekman layer problem, and the inductive diagnostic program (i.e., finding  $K$  by the analysis of field data) seems to have led into a blind alley.

If one had assumed that  $K$  must be real and physical in the sense described at the beginning of this section, then these results could be interpreted to show that classical diffusion theory has been refuted for fair weather, upper ocean conditions. However, even these very weak assumptions on the form of  $K$  seem arbitrary. Moreover, there may be no point in refuting the classical diffusion theory (other than the commendable desire to clear away unsuccessful theories); an apparent failure shows only that we have not yet discovered the appropriate  $K$ . When viewed in this way, diffusion theory is a convention and not a testable scientific theory; it might yet serve as a basis for prediction, given the parameter dependence of  $K$ , but is unlikely to have the depth required of an explanation.

To proceed further with diffusion theory, something has to be added beyond the inductive diagnostic program. We will return to diffusion models in section 6 and attempt to deduce the diffusivity from a new Ekman layer solution that arises from consideration of time dependence and time averaging.

#### 4. Process and Consequences of Diurnal Cycling

Under fair weather conditions the upper ocean is warmed by the Sun and restratified each day [Price et al., 1986; Wijffels et al., 1994, and references therein]. The diurnal cycle of stratification is an important mode of variability in the upper 10 to 30 m of the water column and as Ekman [1905, p. 43] anticipated, is likely to have a marked effect upon diffusivity and thus upon wind-driven currents,

It is obvious that (the eddy diffusivity) cannot generally be regarded as a constant when the density of the water is not uniform within the region considered. For (the eddy diffusivity) will be greater within the layers of uniform density and comparatively small within the transition-layers where the formation of vortices must be much reduced owing to the differences in density.

The striking consequences of the covariation of stratification and diffusivity are evident in the diurnal cycle of current observed under fair weather conditions in

the subtropical North Pacific (Figure 7). During the evening and early morning the upper ocean was neutrally stratified, i.e., was a density mixed layer, to a depth of about 20–30 m. There was comparatively little vertical shear of the hourly averaged current within this density mixed layer (vertical shear remains measurable,  $O(10^{-3}) \text{ s}^{-1}$ , and is generally in the downwind direction). To a first approximation, velocity and density mixed layers were thus coincident. As the surface layer was warmed by solar insolation during late morning, the wind stress became trapped in a warmed surface layer that accelerated downwind and formed a surface-trapped, half jet dubbed the diurnal jet. The diurnal jet was accelerated also by the Coriolis force, which turned it to the right (Northern Hemisphere) in the sense of an inertial motion. The jet grew in amplitude until about sundown, when the surface heat flux changed to cooling. By that time the diurnal jet had turned roughly  $90^\circ$  to the right of the wind stress (along the  $10^\circ\text{N}$  section the rotation would be only about a third of this). During the evening and early morning the jet amplitude was rapidly reduced by vertical mixing associated with the regrowth of the density mixed layer, and when the Sun came up the following day, the initial condition for the next diurnal cycle was a more or less “clean slate” [Stommel *et al.*, 1969].

The thickness and amplitude of the diurnal jet vary with the surface heat flux and wind stress, but the pattern described above repeats every day under fair weather conditions (Figures 8, 9, and 10). From these current and temperature observations we draw three qualitative “rules” useful for modeling the fair weather Ekman layer (relevant upper ocean turbulence measurements are noted).

1. Most of the vertical shear of the wind-driven current occurs in conjunction with stable stratification. Vertical shear within the density mixed layer is comparatively small (though see *Weller and Plueddemann*, [1996]). The latter implies that the eddy diffusivity within the density mixed layer is large,  $O(1000 \times 10^{-4} \text{ m}^2 \text{ s}^{-1})$ , suggesting either intense or large turbulent eddies. (Observations and highly resolved turbulence simulations indicate eddies that sweep through the full thickness of the mixed layer [D’Asaro *et al.*, 1996; D’Asaro and Dairiki, 1997; *Weller and Price*, 1988; *McWilliams et al.*, 1997].)

2. Turbulence and diffusivity within the stratified fluid below the mixed layer are greatly reduced compared with those in the mixed layer. (This is evident in observations of temperature within the diurnal thermocline [Price *et al.*, 1986] and in turbulent dissipation measurements [Brainerd and Gregg, 1993a, b], which show that it is not literally zero.)

3. Under fair weather conditions the thickness of the highly diffusive mixed layer goes through a large-amplitude diurnal cycle [D’Asaro *et al.*, 1996; D’Asaro and Dairiki, 1997; *Brainerd and Gregg*, 1993a, b, and references therein].

The rules above can be implemented most simply within a depth- and time-dependent diffusion model having a prescribed diffusivity. The diffusivity within a mixed layer of thickness  $h(t)$  is made very large,  $K_0 = 1000 \times 10^{-4} \text{ m}^2 \text{ s}^{-1}$ , as a first guess and is assumed to vanish below. The thickness of this mixed layer is made to go through a diurnal cycle (sawtooth form) having a daytime minimum at the sea surface (to avoid introducing a parameter) and a nighttime maximum of 50 m, thus causing a depth- and time-dependent  $K$ ,

$$\begin{aligned} K(z, t) &= K_0 \text{ if } 0 > z > -h(t), \\ K(z, t) &= 0 \text{ otherwise.} \end{aligned}$$

The momentum equation is the time-dependent form (2), and surface and lower boundary conditions are as before. This model is readily solved numerically, and the time-averaged current profile is computed from the solution. Of interest is whether the solution spiral has a more realistic, flattened shape than did solutions of the classical diffusion model. Indeed, it does (Figure 11), and the amplitude is realistic as well. An important result of sensitivity experiments is that solutions of this model are almost independent of  $K_0$ , provided that it is at least as large as the value  $1000 \times 10^{-4} \text{ m}^2 \text{ s}^{-1}$  used here. This is a remarkable simplification over the classical diffusion models, in that a realistic solution emerges from implementing three, largely qualitative rules.

To appreciate some of the consequences of a time- and depth-varying  $K$ , it is helpful to examine a Reynolds decomposition of the mean stress,

$$\overline{\tau} = K \frac{\partial \overline{v}}{\partial z} = K' \frac{\partial v'}{\partial z} + \overline{K} \frac{\partial V}{\partial z},$$

and where  $v = V + v'$ , as before. The mean term (second term on right-hand side) is analogous to the classical diffusion parameterization (7), in that it is proportional to the shear of the mean current. The eddy term (first term on the right-hand side) is as large as the mean term and is not parallel to it or to the mean stress (Figure 12). Thus it is evident that an accurate parameterization of the mean stress, given only the mean current, will require a complex diffusivity having a significant rotation (small near the surface and increasingly positive at depth, averaging  $\sim \pi/4$ ). This is consistent with the diffusivity diagnosed from observations in section 3.3 and, as we have implied before, consistent also with the flattened shape of the fair weather spiral.

## 5. Layered Model of Diurnal Cycling

The previous results suggest that one way to arrive at a physically based model of the fair weather Ekman layer might be to solve for the time average of an upper ocean that is subject to diurnal cycling. The full problem has mixed time and space dependence and proba-

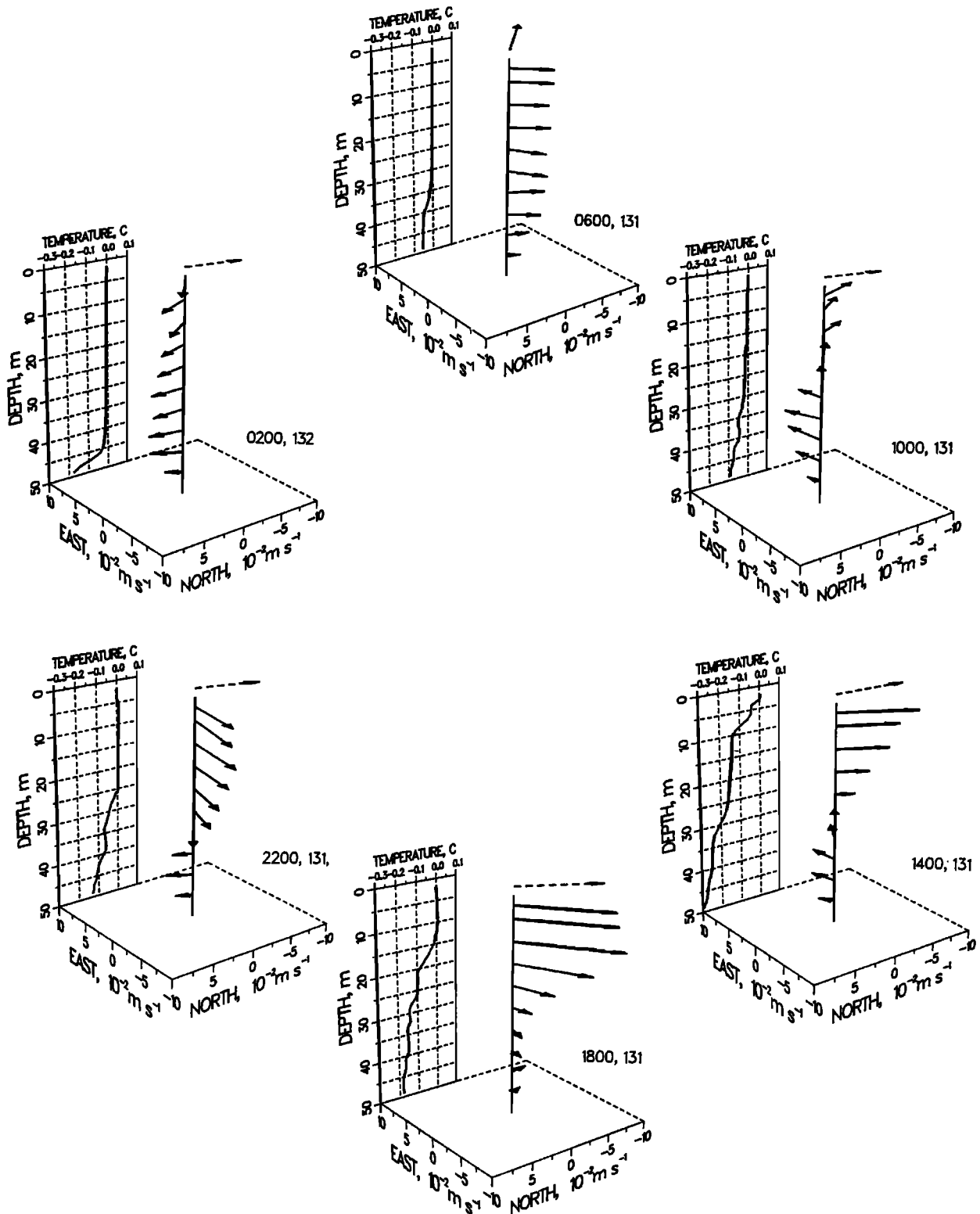


**Figure 7.** An observed diurnal cycle of temperature and current from *Price et al.* [1986]. Currents were measured by vector-measuring current meters, smoothed over 30 min at a given depth and referenced to 50 m depth. Temperature was measured by conductivity-temperature-depth (CTD) profilers and referenced to the sea surface. The uppermost dashed vector shows the wind stress direction.

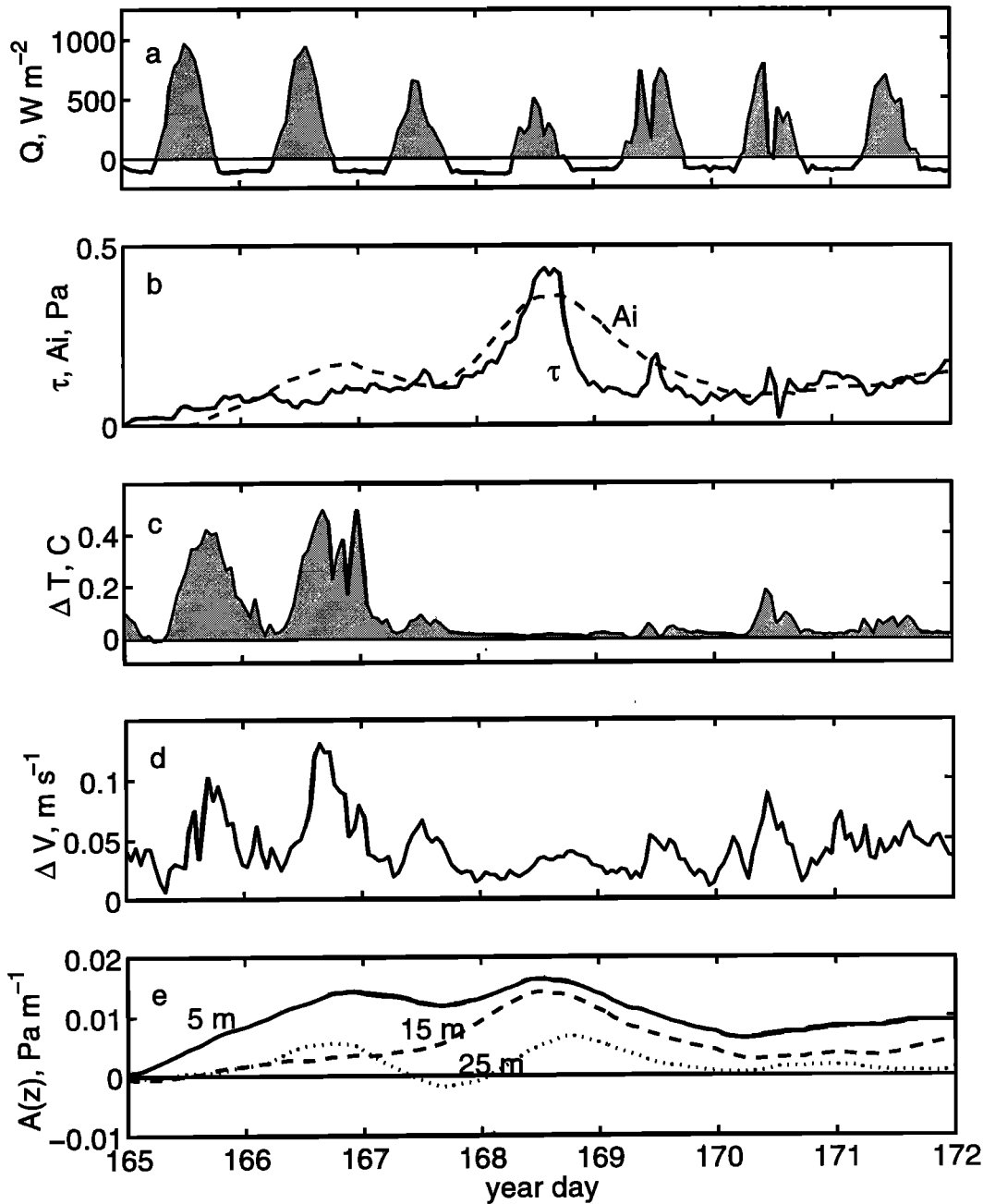


**Figure 8.** A weeklong segment of data from LOTUS3 chosen when wind direction was fairly steady and there was no strong mesoscale variability. The time is in local year day, with 165 being mid-June. (a) Net heat flux, with warming periods shaded. (b) Wind stress magnitude (solid line) and the integrated geocentric acceleration ( $A_i$ ) (dashed line) estimated from current measurements (as in the work by Davis *et al.* [1981a]) and smoothed with an 18-hour running mean. Wind direction (not shown) was more or less steady toward the northeast. (c) Temperature difference between the sea surface (0.6 m) and 10 m. (d) Velocity difference (magnitude only) between 5 and 10 m. Note that the velocity difference shows a marked diurnal variability, with the largest velocity difference usually occurring just after noon, consistent with the maximum of the diurnal jet. (e) Geocentric acceleration  $A(z)$  at depths of 5, 15, and 25 m (solid, dashed, dotted lines, respectively) smoothed with an 18-hour running mean. The vertical integral  $A_i$  is in Figure 8b, where it can be compared to the wind stress.

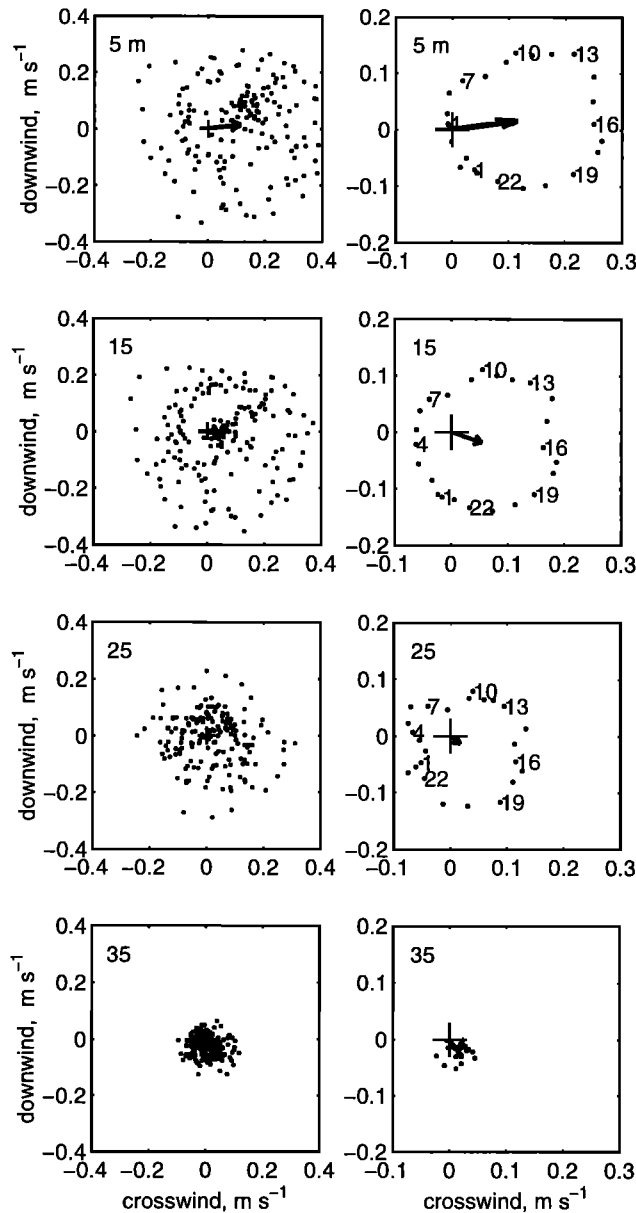


**Figure 9.** Current hodographs from a weeklong segment of LOTUS3 data. (left) Hourly averaged current (dots) at 5, 15, 25, and 35 m depth and the time-averaged current (the small central vector) shown in a downwind and crosswind coordinate system. (right) Ensemble, diurnal-averaged currents (note the scale change compared to the left column). The roughly circular array of dots denotes the velocity vector at hourly intervals, every third of which is labeled (local time). Thus the diurnal maximum at 5 m depth occurs at  $\sim 16L$ , when the current is flowing  $\sim 90^\circ$  to the right of the wind stress. The small central vectors show the time-averaged current. Note that the time-averaged current at 5 m depth is about half the magnitude of the diurnal cycle, while at 25 m depth the time-averaged current is much smaller than the diurnal cycle, the latter being a near-inertial oscillation.

bly requires numerical solution as above. However, the observations and results above suggest further simplifications that will lead to a simple, explicit solution.

### 5.1. Model Formulation and Integration

As an approximation one could assume that the diffusivity within the density mixed layer is effectively infinite, i.e., that the density mixed layer is also a velocity mixed layer. Going further and taking the lower interface of the mixed layer to be steplike gives a two-layer form of the momentum equations in which wind stress is absorbed entirely within a density mixed layer of time-varying thickness  $h(t)$ ,

$$\frac{\partial \mathbf{v}}{\partial t} + i f \mathbf{v} = -W_e \frac{\delta \mathbf{v}}{h} + \frac{1}{\rho h} \boldsymbol{\tau}. \quad (13)$$

The entrainment velocity  $W_e = \partial h / \partial t$  when  $\geq 0$  and vanishes otherwise. The velocity difference  $\delta \mathbf{v}$  is taken across the base of the mixed layer. The fluid below the mixed layer is enforced,

$$\frac{\partial \mathbf{v}}{\partial t} + i f \mathbf{v} = 0, \quad (14)$$

which holds down to  $z = -H$ , the deepest extent of the mixed layer and Ekman layer.

A crucial part of the problem is to specify the stratification represented by the depth of semipermanent stratification  $H$  and the time-varying mixed-layer depth  $h(t)$ .  $H$  is presumed to be the top of the seasonal or main thermocline and is thus set by processes that may be inherently nonlocal, as for example, the east-west tilt of the tropical Pacific thermocline [Wijffels *et al.*, 1994]. For now,  $H$  is taken to be given and steady so that we can emphasize the effect of time-varying  $h(t)$  (variable  $H$  will be considered in section 7 and shown to be important, especially in the tropics). In fair weather conditions the variation of mixed-layer depth  $h(t)$  will be associated primarily with the diurnal cycle. To model the consequences of this variation, we make the simplifying assumption that  $h$  varies with a top-hat time dependence over the course of a day, though the actual time dependence is smoothly varying, especially evident in the afternoon deepening phase (Figure 7). The nighttime mixed-layer depth is taken to be the given depth of semipermanent stratification,

$$h_{\text{night}} = H,$$

while the shallower, daytime mixed layer depth is taken to be the so-called trapping depth of Price *et al.* [1986],

$$h_{\text{day}} = D_Q = \frac{U_*^2 P_\tau}{\sqrt{Q_* P_Q / 2}}, \quad (15)$$

where  $P_\tau = (1/f)\sqrt{2 - 2\cos(fP_Q/2)}$ ,  $Q_* = g\beta Q / (\rho C_p)$  [ $l^2 t^{-3}$ ], with  $g$  the acceleration of gravity,  $\beta$  the thermal expansion coefficient, and  $C_p$  the heat capacity of seawater (constant for a given case);  $Q$  is the daily maximum surface heat flux, and  $P_Q$  is the period over which the net surface heat flux is warming. We are assuming an idealized surface heat flux that oscillates diurnally



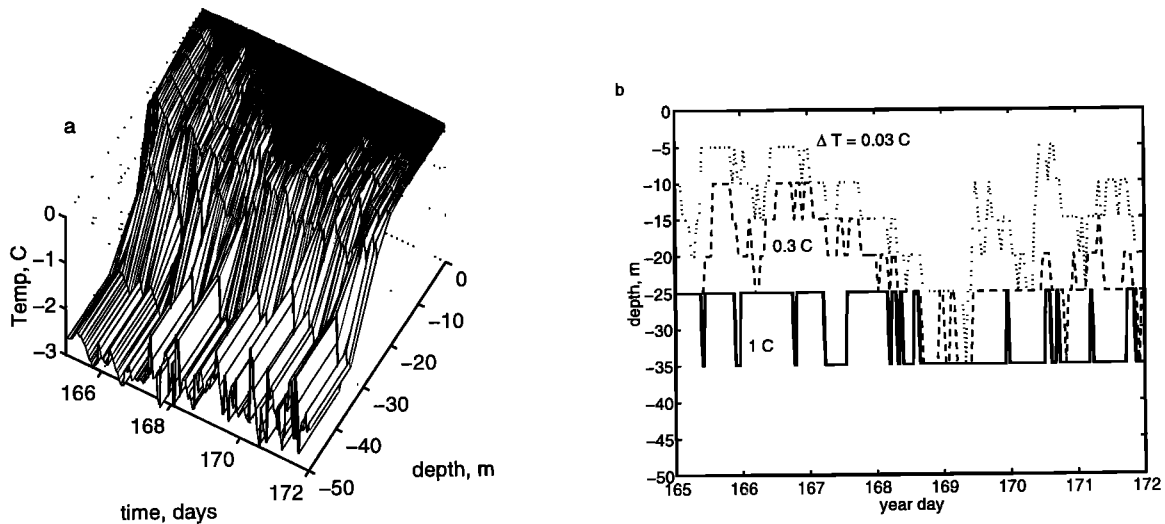


**Figure 10.** Temperature measured by vector-measuring current meters referenced to the surface in order to show the changing depth of stratification during the weeklong period shown in Figures 8 and 9. (a) Temperature displayed as a contoured surface. (b) Depth where the temperature changed (decreased) from the surface value by  $0.03^{\circ}\text{C}$  (dotted line),  $0.3^{\circ}\text{C}$  (dashed line), and  $1^{\circ}\text{C}$  (solid line). These time series have rather coarse depth resolution set by the depths of the current meters.

with zero long-term mean to produce closed diurnal cycles.  $Q$  is thus a measure of the variability of the surface heat flux, which is extremely important because heat and cooling have quite distinct and asymmetric effects upon the upper ocean. If the diurnal cycles are closed and repeating, then the interval  $P_Q$  used by Price *et al.* [1986] can be approximated by half a day,  $P_Q \approx \pi\Omega^{-1}$ , where  $\Omega = 2\pi \text{ day}^{-1}$ , and for this purpose,  $\Omega \approx (4\pi/f)\sin(\phi)$ , where  $\phi$  is the latitude. The depth  $D_Q$  is termed the diurnal warm layer depth or thickness and derives from a bulk Richardson number condition upon the shear and stratification of the diurnal

warm layer. (That  $h_{\text{day}}$  should be strictly equal to  $D_Q$  is not obvious a priori as noted below.) This  $D_Q$  is analogous to the diffusive depth  $D_K$  of the classical diffusion model (section 3.2), but note that  $D_Q$  depends only upon external variables. It can be evaluated for the three cases considered here, and  $D_Q = 13, 17,$  and  $25\text{ m}$  for LOTUS3, EBC, and  $10^{\circ}\text{N}$ , respectively. This can be compared to the observed e-folding depth of the current speed, 10, 16, and 32 m (Table 1), though the analogy is not complete (more on this in section 5.5).

Given that the stratification is specified, the remaining task is to integrate the momentum equations and

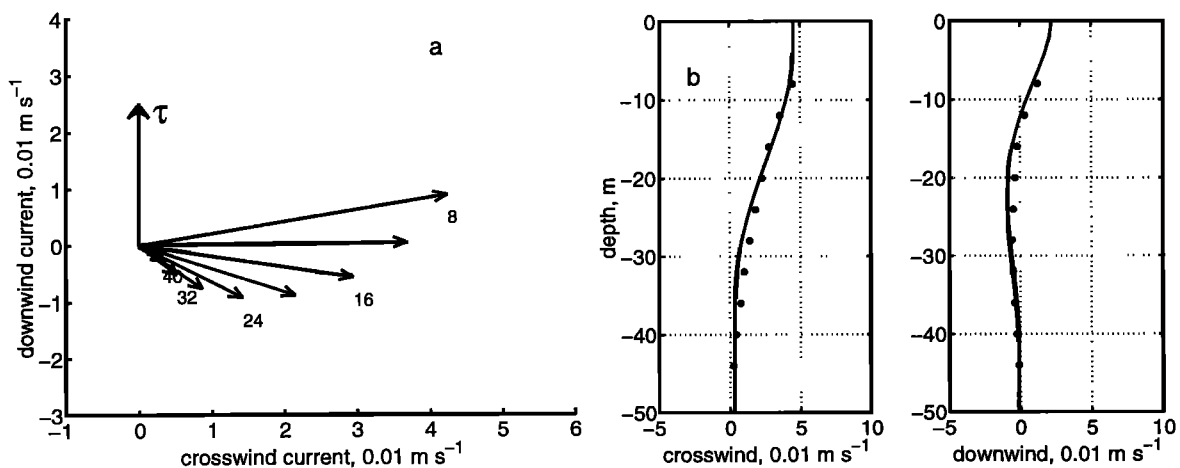


**Figure 11.** Solutions of the depth- and time-dependent diffusion model. External parameters were set to those of the EBC case, and the mixed layer diffusivity was  $K_0 = 1000 \times 10^{-4} \text{ m}^2 \text{ s}^{-1}$ . (a) Solution hodograph that can be compared to Figure 1c. (b) (left) Crosswind and (right) downwind currents that can be compared with EBC data shown as the discrete points.

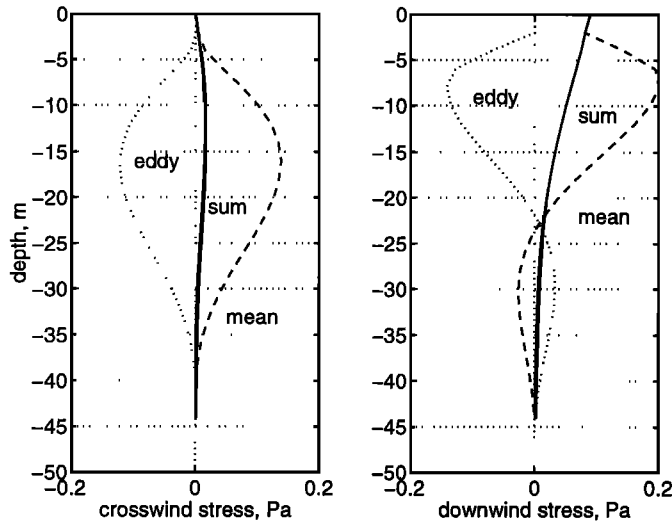


**Figure 12.** Stress profiles (solid lines) and their Reynolds decomposition into mean (dashed lines) and eddy (dotted lines) components computed from the solutions of the depth- and time-dependent diffusion model. Note that the eddy component is as large as the mean component and that the eddy and mean terms almost cancel in the crosswind direction. If they had canceled completely, the current spiral would be entirely flattened in the downwind direction.

then time average the solution (rather than time average the momentum equation). This can be greatly simplified by noting that vertical shear will occur only when the diurnal stratification is “on”, i.e., when  $h = D_Q$ . Otherwise, the current profile is vertically homogeneous above  $z = -H$ . The initial condition for the diurnal jet is thus a vertically uniform current profile. The vertical shear of the subsequent wind-driven current is then independent of the initial condition, and the shear follows the Fredholm solution for the impulsive start-up of a layer of thickness  $h = D_Q$ , forced by a wind stress switched on at  $t = 0$ ,

$$\delta v = \frac{U_*^2}{fD_Q} [1 - \exp(-ift)] = U_Q \psi. \quad (16)$$

This holds for half a day,  $t = \pi\Omega^{-1}$ , after which the shear vanishes along with the diurnal warm layer. The scale

$$U_Q = \frac{U_*^2}{fD_Q} = \frac{\sqrt{Q_* \pi \Omega^{-1}/2}}{fP_\tau} \quad (17)$$

is the amplitude of the diurnal jet and  $\psi$  is plotted in Figure 13. So far as the vertical shear is concerned, each day is the same as the last and thus the time-averaged shear is equal to the shear averaged over just 1 day,

$$\delta V = \frac{U_Q}{2\pi\Omega^{-1}} \int_0^{\pi\Omega^{-1}} \psi dt = U_Q \Psi. \quad (18)$$

The time-averaged  $\psi$  is

$$\Psi = \frac{1}{2} + \frac{i}{4\pi\sin(\phi)} \{1 - \exp[-i2\pi\sin(\phi)]\}, \quad (19)$$

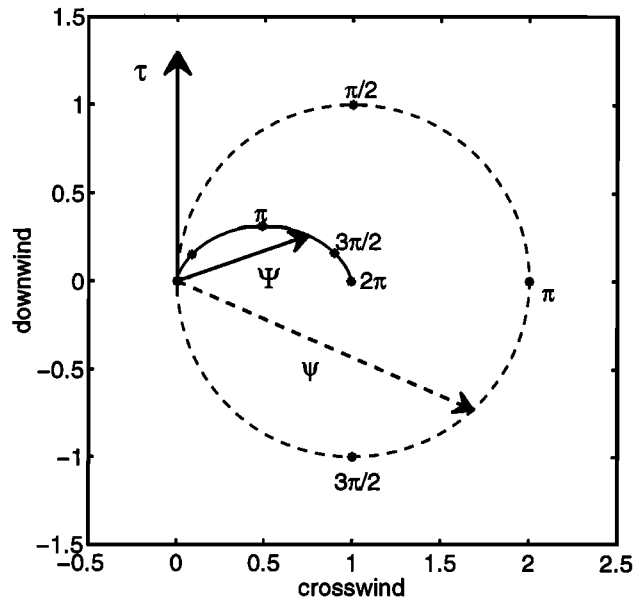


**Figure 13.** The hodograph of a (normalized) wind-driven current  $\psi$  (the dashed vector) forced by a northward wind stress switched on at time = 0 given by equation (16). The time average of this current over 1 day is the shorter (solid) vector  $\Psi$  given by (18). The shear follows this solution, provided that the current profile just before the onset of diurnal stratification is depth independent. The current vectors shown here are for the phase  $ft = 2\pi\sin(\phi) = 1.2\pi$  appropriate to LOTUS3 and EBC. Thus the time-averaged shear is expected to be roughly  $75^\circ$  to the right of the wind stress at LOTUS3 and EBC. The total surface current is very similar in those cases since the shear constraint dominates the solution (Figure 14a).

a function of latitude alone, and is also plotted in Figure 13. Equation (18) will be referred to as the shear constraint. A second integral comes from noting that the time-averaged transport above  $z = -H$  must be the Ekman transport, regardless of stratification and diurnal cycling and thus

$$V_1 D_Q + V_2 (H - D_Q) = \frac{U_*^2}{f}, \quad (20)$$

which will be referred to as the transport constraint.  $V_1$  is the current above  $z = -D_Q$  and  $V_2$  is the current from  $-H < z < -D_Q$ . The time-averaged current follows immediately,

$$V(z') = U_H [1 + (\alpha c(z') - 1)\Psi], \quad (21)$$

where  $U_H = U_*^2/fH$  as in the CLDM solution and where

$$\alpha = H/D_Q = \frac{H\sqrt{Q_*\pi\Omega^{-1}/2}}{U_*^2 P_\tau},$$

which is analogous to the ratio  $H/D_K$  of the CLDM. The depth  $z' = z/H$ , and  $c$  is a flag that turns on or off depending upon depth;  $c = 1$  if  $\alpha z' > -1$  (within the diurnal warm layer, layer 1) and  $c = 0$  if  $\alpha z' < -1$  (below the diurnal warm layer, layer 2). This solution depends only upon external parameters and can be evaluated readily (Figure 14).

For some purposes, e.g., examining the parameter dependence of the surface current, this two-layered, stratified Ekman layer solution, termed SEL2, could be considered complete. However, for most practical purposes it is useful or even necessary to make the solution at least semicontinuous with depth. This can be done in two different ways; by defining the equivalent diffusion parameterization (taken up in section 6) or by the addition of layers.

## 5.2. Some Additions and a Check

The two-layer model, taken literally, indicates a velocity jump between the layers. There is, of course, no such velocity jump found in the ocean, nor in any highly resolved upper ocean model. To represent the interface between these layers, a third layer of thickness  $D_Q$  is inserted between layers 1 and 2, and the current in this intermediate layer is computed by a linear interpolation in the depth range  $1/2 D_Q < -z < 3/2 D_Q$ . Another velocity jump occurs at the bottom of the Ekman layer,  $z = -H$ . At subtropical or higher latitudes this velocity jump will usually be quite small. However, at lower latitudes the deep Ekman layer currents can be fairly large,  $O(0.1 \text{ m s}^{-1})$ , and cause significant mixing. To simulate this feature, a fourth (and final) layer is added to the bottom of the Ekman layer. The thickness of layer 4 is set by a critical gradient Richardson number condition (but as we will discuss shortly, the lower interface layer evident in the observations is much thicker than this yields). The embellished, semicontinuous solution has four distinct layers, two uniform and two sheared, and is termed SEL4 (four-layer stratified Ekman layer).

The dynamics represented by SEL4 are a subset of the dynamics in the Price *et al.* [1986] upper ocean numerical model (PWP), and SEL4 could be regarded as an approximate solution for idealized surface fluxes. To check the approximations made during the derivation of SEL4, it is useful to compare SEL4 with time-averaged solutions computed from the PWP numerical model (Figure 15). From this it would appear that SEL4 is a faithful rendition of the PWP physics, which is all that could have been expected. (It is notable that SEL2 is an Ekman layer solution free of tunable parameters and similarity constants (though the addition of layers 3 and 4 to make SEL4 represented a gross and ad hoc adjustment of the profile structure). This must be fortuitous because there was no way to assert a priori two of the approximations used in the derivation.

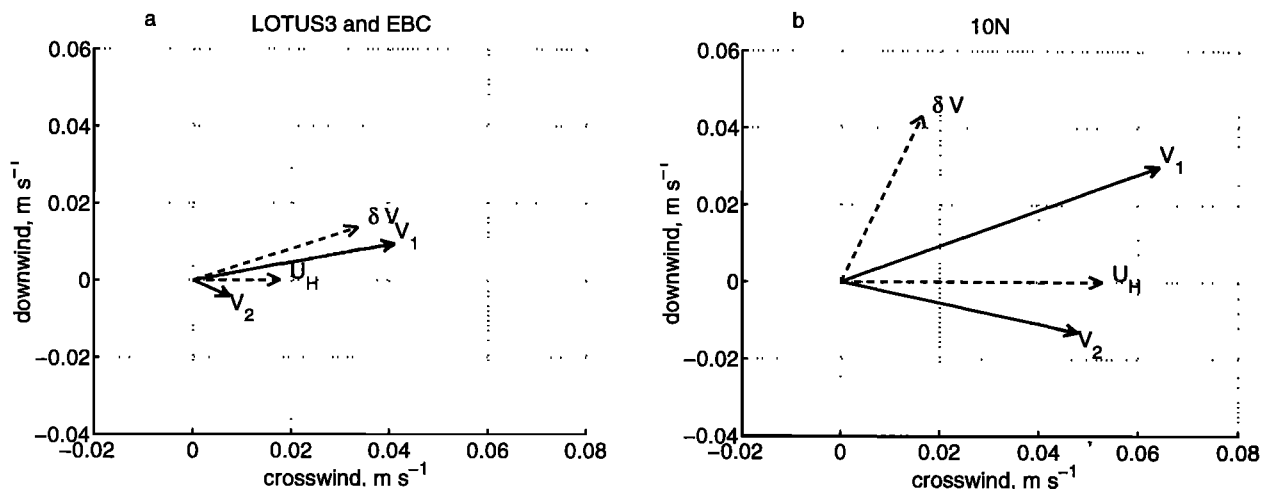


**Figure 14.** Solutions of SEL2 for external parameters of (a) LOTUS3 (very nearly EBC) and (b) 10°N. The wind stress (not shown) is due "north."

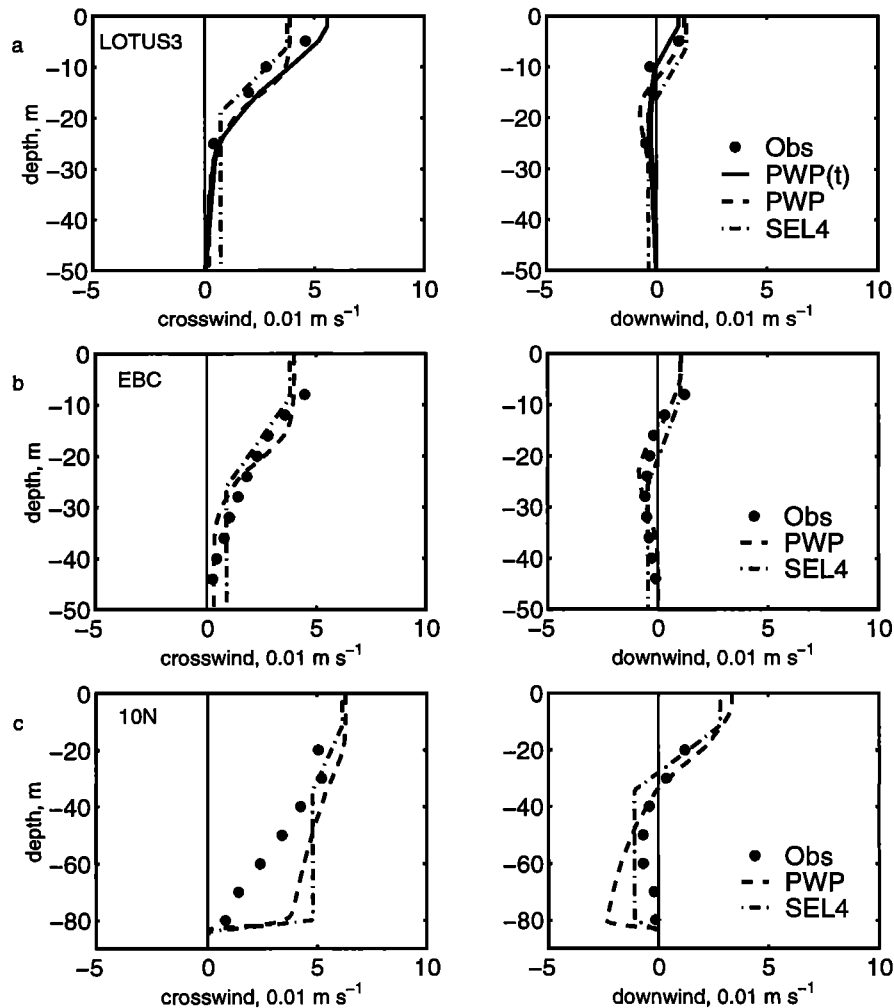


**Figure 15.** Comparisons of the SEL4 solution (dash-dotted lines) with the PWP numerical solution (dashed lines), and in the LOTUS3 case only, with the PWP numerical model run using the hourly surface fluxes (solid line) for (a) LOTUS3, (b) EBC, and (c) 10°N. The solid dots are the observations.

Specifically, the trapping depth was expected to be proportional to the thickness of the diurnal warm layer but not necessarily equal to it, and in the same way the top-hat time dependence assumed for the diurnal variation of the mixed layer depth can only be approximate. During the initial development of the SEL2 solution it was presumed that the time during which  $h = h_{\text{day}}$  should be set equal to  $\gamma\pi\Omega^{-1}$ , with  $\gamma$  expected to be roughly 1, but made available as an adjustable parameter. Subsequent comparison of SEL2 and SEL4 with PWP numerical solutions showed that the optimum choice,  $\gamma = 1.1$ , gave only a very slightly enhanced fit to the numerical solutions, and hence  $\gamma$  was omitted. The SEL2 solution is approximate for other reasons, including that optical properties are ignored.)

### 5.3. Comparison With Observations

Given the surface fluxes of momentum and heat and assuming that the depth of semipermanent stratifica-

tion is known from climatology or direct observation, then the SEL4 solution can be evaluated unambiguously and compared directly with observations (Figure 5). In the subtropical cases the agreement appears to be fairly good visually, and notice, in particular, that these solutions have a flattened spiral shape,  $F_v \approx 2.5$ , that proved difficult for the classical diffusion model. For the LOTUS3 case the rms vector error is  $0.008 \text{ m s}^{-1}$  and the percent variance accounted for by the SEL4 solution is  $\text{PV} = 90\%$ . For the EBC case the rms vector error is  $0.005 \text{ m s}^{-1}$  and PV is a little more than 90%. These are slightly better than the optimum CLDM solution (Table 2).

The SEL4 solution is less successful in the 10°N case: The rms vector error is  $0.019 \text{ m s}^{-1}$ , and PV is only 73% (still a little better than the optimum CLDM solution). Almost all of the error comes from depths of 50–70 m, where the SEL4 solution overestimates the crosswind currents. An error of that sense is bound to occur somewhere in the water column since the predicted Ekman

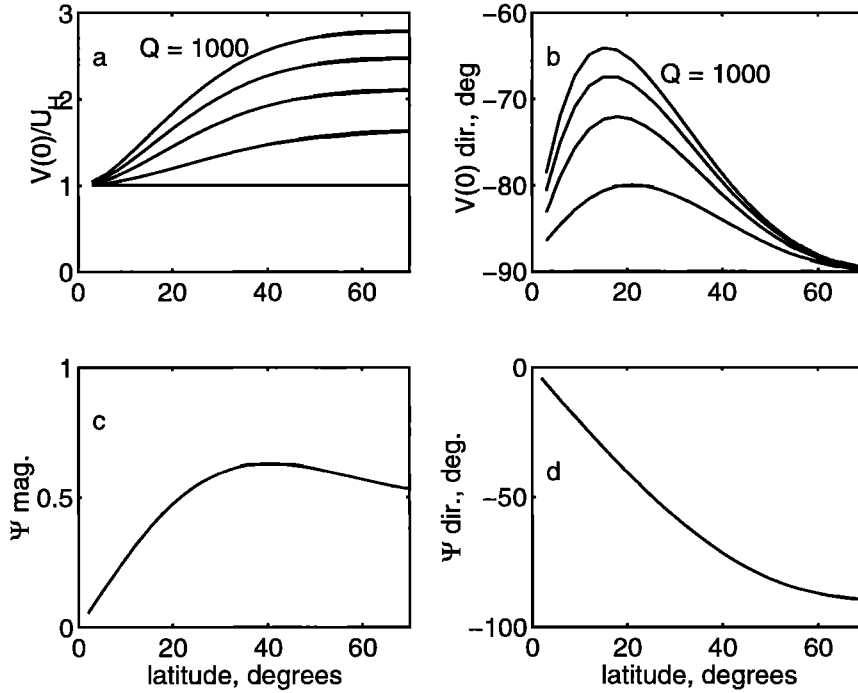


**Figure 16.** Parameter dependence of the SEL2 surface current (same as SEL4). (a) Speed of the surface current normalized by the neutral velocity scale for  $\tau_w = 0.1$  Pa,  $H = 50$  m (held fixed), and  $Q = 250, 500, 750,$  or  $1000$  W m<sup>-2</sup> and as a function of latitude. Speeds greater than 1 show some effect of diurnal cycling. (b) The direction of the surface current with respect to the wind stress (negative direction is to the right of the wind stress). The surface current is at nearly right angles to the wind stress for conditions of very low heating, in which case there is no effect of diurnal cycling, and also at very low and very high latitudes, regardless of the heating. (c) Amplitude and (d) phase of  $\Psi$ . Recall that the time-averaged shear due to diurnal cycling is proportional to  $\Psi$ .

transport exceeds the measured transport by some 30%. (If the wind stress is reduced by 30% so that the predicted transport matches the observed transport, then the rms misfit of SEL4 is  $0.009$  m s<sup>-1</sup> and  $PV = 94\%$ . Recall the similar improvement in the statistical fit of the CLDM solution, section 3.2.) Even with allowance for the transport discrepancy in the 10°N data set, it remains that the shear across the base of the Ekman layer is much too abrupt (the same error is evident in the CLDM solutions (Figure 5) and is likely due to the lower boundary condition, section 7).

#### 5.4. Parameter Dependence of SEL2

Before discussing parameter dependence in detail, it is helpful to consider what SEL2 (or 4) has added to the list of relevant external variables. The absolute minimum set of relevant external variables that would appear in a model of the Ekman layer current  $U$  would surely include  $z, U_*, f,$  and  $H$ . A nondimensional solution could then be written in the form

$$\frac{U}{U_H} = \text{function}(z', \alpha)$$

where  $z' = z/H$  and  $\alpha = H/D_K$ , with  $D = \sqrt{2K/f}$  or  $\propto U_*/f$ , the latter corresponding to the parameterized CLDM solution. Explicit treatment of the diurnal cycle and time averaging introduced two new external variables,  $Q_*$  and  $\Omega^{-1}$ , and the solution would then be

$$\frac{U}{U_H} = \text{function}(z', \alpha, f/\Omega)$$

where  $z'$  and  $\alpha = H/D_Q$  have much the same roles as in the diffusion theories, while  $f/\Omega \propto \sin(\phi)$  is new. This additional, separate dependence upon latitude sets the SEL2 solution apart from classical diffusion theories and admits flattened (or not) spirals.

**5.4.1. Heating and wind stress.** Heating and wind stress affect the structure of the SEL2-predicted Ekman layer in a straightforward way that follows from the  $\alpha$  dependence noted above. It is evident from (21) that when  $\alpha = H/D_Q \rightarrow 1$ , the effects of diurnal cycling will be negligible. In that limit the surface current and the deep current (layers 1 and 2) both go to the null model

$$\mathbf{V} = U_H, \quad (22)$$

as in the vanishing  $\alpha$  limit of the CLDM, (10), and Figures 3a–3c. This is an important limit about which this model has nothing interesting to say (see, instead, *Gnanadesikan and Weller [1995]* and *McWilliams et al. [1997]*).

The SEL2 solution is relevant in the limit,  $\alpha \geq 1$ , or in terms of external parameters,

$$\frac{\sqrt{Q_*\pi\Omega^{-1}}H}{U_*^2 P_\tau} \geq 1, \quad (23)$$

which defines “fair weather” for our purposes. In this limit the effect of diurnal cycling on the Ekman layer structure may be substantial, but, to tell for sure, the upper layer current has to be compared to the neutral velocity scale  $U_H$ , and this depends upon both  $\alpha$  and the latitude through the phase  $\Psi$  (the amplitude of which is in Figure 16c). Outside of the tropics,  $\phi \geq 30^\circ$  and assuming that  $\alpha \gg 1$ , then the layer 1 current is determined by the shear constraint alone,

$$V_1 \approx U_Q \Psi = \frac{\sqrt{Q_*\pi\Omega^{-1}/2}}{fP_\tau} \Psi, \quad (24)$$

and the speed is independent of the wind stress (the warm layer thickness is proportional to the wind stress, and thus the speed of the diurnal jet is independent of the wind stress [*Price et al., 1986*]). The subtropical cases are close to this limit, as can be seen in Figure 4a. The speed computed from (24) is  $\approx 0.04 \text{ m s}^{-1}$ , and the direction of  $\Psi$  is  $\sim 75^\circ$  to the right of the wind stress (Figure 13), both of which are consistent with the shallowest observed currents at LOTUS3 or EBC (Figures 1a and 1c). Thus the SEL2 solution gives a slightly surprising explanation of a fairly ordinary fact.

Aside from the near-equatorial region, most days and most places will fall between the neutral and fair weather extremes noted above and the SEL2 surface current will depend upon both  $H$  and  $D_Q$ . The stress dependence of the surface current will then be intermediate as well.

The sensitivity to errors in the surface fluxes can be evaluated by calculating perturbed solutions in which  $\tau$  and  $Q$  are varied by a nominal uncertainty, 20%, and then computing the PV between the nominal and perturbed solutions. For midlatitude conditions,  $\tau$  uncertainty of 20% gives PV = 95 (88)%, where the value in parentheses is for the depth-dependent part. For  $10^\circ\text{N}$  conditions, PV = 96 (68)% or comparable to the errors found in the best models. The sensitivity to the heat flux is much less, PV = 99 (97)% for middle or tropical latitudes. Errors in the estimated heat flux are probably not a major contributor to error in the simulations, while error in wind stress clearly could be, especially in the tropics.

In any field data set the meteorological conditions are bound to vary from day to day, so that the surface fluxes must also vary from day to day. It has been assumed implicitly that the surface fluxes could be represented

by their averaged values, i.e., the time-averaged wind stress and the average of the daily maximum heat flux. However, the SEL4 solution is not linear in these variables, and hence the use of averaged fluxes must induce an error in the simulations of field data. To get a sense of the magnitude, we have computed the average current over an ensemble of solutions in which  $\tau$  was varied from 0.05 to 0.25 Pa while  $Q$  was simultaneously varied from 300 to 800  $\text{W m}^{-2}$  and compare this ensemble-averaged solution (which could always be computed if the surface fluxes were known in detail) to the single solution computed from the averages of  $\tau$  and  $Q$  (Figure 17a). The error induced by the use of the averaged surface fluxes appears to be small compared to the typical current (less than 10% over most of the Ekman layer) and within the uncertainty associated with current sampling or stress estimation. Interestingly, the use of an averaged  $H$  may lead to somewhat larger errors (section 7).

**5.4.2. Latitude.** An important result is that the effects of diurnal cycling on the Ekman layer are expected to be lessened at tropical latitudes because the depth-averaged current  $U_H$  overwhelms the shear associated with the diurnal cycle. The ratio of the shear to  $U_H$  is  $U_Q\Psi/U_H \approx \alpha\pi^2\sin(\phi)$ , which vanishes as the latitude  $\phi$  goes to zero. In essence,  $U_Q\Psi$  has a finite upper limit (0.07  $\text{m s}^{-1}$  is about as large as it can be) while  $U_H$  will increase without bound as latitude goes to zero (ignoring nonlocal dynamics). This tendency is evident already in the  $10^\circ\text{N}$  solution (Figure 5c, right), where the effect of diurnal cycling is to cause the nearly downwind shear of the current at depths of around 10 to 25 m. This shear is not large compared to the depth-averaged Ekman layer current  $U_H$  (Figure 12b, right). Thus Ekman layer structure in the tropics appears to be set mainly by the depth of semipermanent stratification (the top of the seasonal or main thermocline) [also see *Chereskin et al., 1997*] rather than by the effects of diurnal cycling that have been emphasized up until now.

In the fair weather, extratropical limit described above, the Ekman transport occurs mainly within the diurnal warm layer, and in the LOTUS3 and EBC cases the ratio  $U_1 D_Q / (U_*^2 / f) = (\Psi_\tau(\alpha - 1) + 1) / \alpha \approx 0.7$ . In the tropics the Ekman transport is much less strongly surface trapped, and in the  $10^\circ\text{N}$  case the same ratio is  $\sim 0.3$ .

The direction of the surface current also has a lively dependence upon  $\alpha$  and latitude, much of which follows from the discussion above. For a given latitude the angle approaches  $-90^\circ$  as  $\alpha$  goes to 1 (weak heating in Figure 16a) and the solution goes to the null model. The angle becomes more positive (that is, the surface current is more downwind) with increased heating. The minimum angle between the wind stress and the surface current is  $\sim -65^\circ$  and occurs at a latitude of  $\sim 10^\circ$  when the heating is very strong (i.e., when  $\alpha \gg 1$ ). The surface current is at nearly right angles to the wind

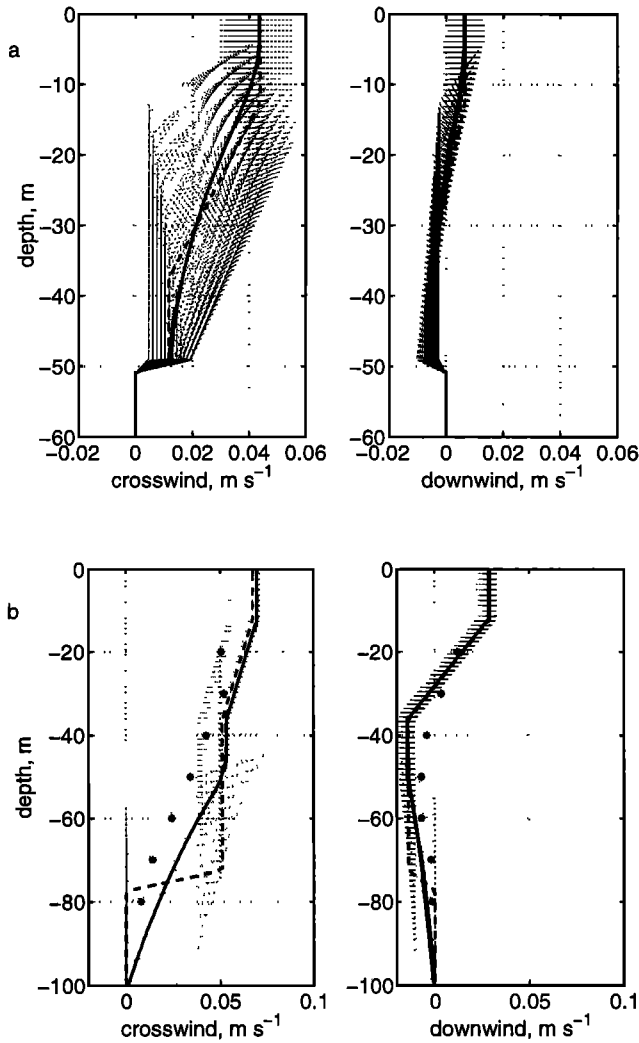


**Figure 17.** Ensemble-averaged solutions of SEL4. (a) (left) Crosswind and (right) downwind current components computed from SEL4 for midlatitude conditions ( $f$  and  $H$  of LOTUS3) with varying  $\tau_w$  over the range 0.025 to 0.25 Pa and  $Q$  over the range 300 to 800  $W m^{-2}$ . The thin dotted lines are the individual solutions; the thick solid line is the ensemble average of these solutions, and the thick dashed line is the solution for the average  $\tau$  and  $Q$ . These two averaged current profiles are fairly similar in this example, suggesting that the use of averaged surface fluxes induces acceptable errors. (b) Tropical conditions ( $f$ ,  $\tau_w$ , and  $Q$  of 10°N) and with  $H$  varying from 50 to 100 m (thin dotted lines). In this example there are rather large differences between the ensemble-averaged solution (solid line) and the solution computed from the average  $H$  (dashed line) within the lower half of the Ekman layer. The upper half of the Ekman layer is nearly unaffected. The ensemble-averaged solution has the qualitative shape of the observed profile (solid dots), but somewhat greater amplitude and transport.

at very low and at very high latitudes, even for the strongest possible heating. At very low latitudes the shear will be almost directly downwind (Figure 15d and the 10°N example noted above) but small compared

to  $U_H$ , and thus the contribution of the shear to the surface current vanishes as  $f$  vanishes. At high latitudes the inertial rotation of the diurnal jet will bring the jet amplitude back to near zero at the end of the heating period (phase  $\approx 2\pi$  in Figure 13), and thus the time average of the shear and the current will be at nearly right angles to the stress throughout the Ekman layer.

## 6. A Complex Laminar Diffusion Model

Given what we have learned to this point, it should be possible to deduce an improved diffusion model, dubbed the complex laminar diffusion model or C<sub>X</sub>LDM. Like the classical diffusion models of section 3, the C<sub>X</sub>LDM attempts to parameterize the mean stress from the mean shear; but unlike the classical models, the C<sub>X</sub>LDM will allow that the mean stress and the mean shear may not be parallel by admitting a complex diffusion coefficient,  $K = K \exp(i\Upsilon)$ , where  $\Upsilon$  is the angle between the shear and the stress. This new diffusion model may be useful for some practical purposes, and its development helps to complete the discussion of diffusion theory left open at the end of section 3.

The solution to the steady momentum equation with boundary conditions as before and with this complex diffusivity is given by (7), though with the coefficient  $\tau = \exp[i(\pi/4 - \Upsilon/2)]$ . Solutions for EBC parameters (Figure 18a) show that a larger positive  $\Upsilon$  causes the current spiral to become increasingly flattened, with  $\Upsilon = \pi/2$  giving a completely flattened spiral having  $F_l \rightarrow \infty$ . Recall that the angle between shear and stress diagnosed from the EBC observations was roughly  $\Upsilon \approx \pi/4$  (section 3.4), which gives a spiral somewhat similar to that observed. An angle  $\Upsilon < 0$  gives solutions with  $F_l < 1$ . The C<sub>X</sub>LDM solutions satisfy the Ekman transport relation exactly.

The intent is that C<sub>X</sub>LDM should be useful for practical purposes, and so it is essential to specify the diffusivity in terms of external parameters. To do this, the complex diffusivity is evaluated by analogy with the SEL2 solution. The simplest case to consider is the large  $\alpha$ , midlatitude limit, wherein diurnal cycling is of greatest importance and  $H$  effectively drops out of the problem. In that event the diffusive depth scale can be equated plausibly with the diurnal warm layer depth; that is,  $D_K = D_Q$ , from which  $K$  magnitude is computed and the angle  $\Upsilon$  is estimated from the known angle between stress and shear of the SEL2 solution, thus

$$K = \frac{fU_*^4 P_\tau^2}{Q_* \pi \Omega^{-1}} \exp\left[i\left(\frac{\pi}{2} - \text{atan}\left(\frac{\Psi_i}{\Psi_\tau}\right)\right)\right], \quad (25)$$

with  $\Psi$  from (19). Notice that the C<sub>X</sub>LDM diffusivity has been presumed to be depth independent or laminar. On the other hand, the complex diffusivity diagnosed from observations (section 3.3) or time-dependent solutions (section 4) indicated a diffusivity magnitude that decreased with depth and an  $\Upsilon$  that increased with

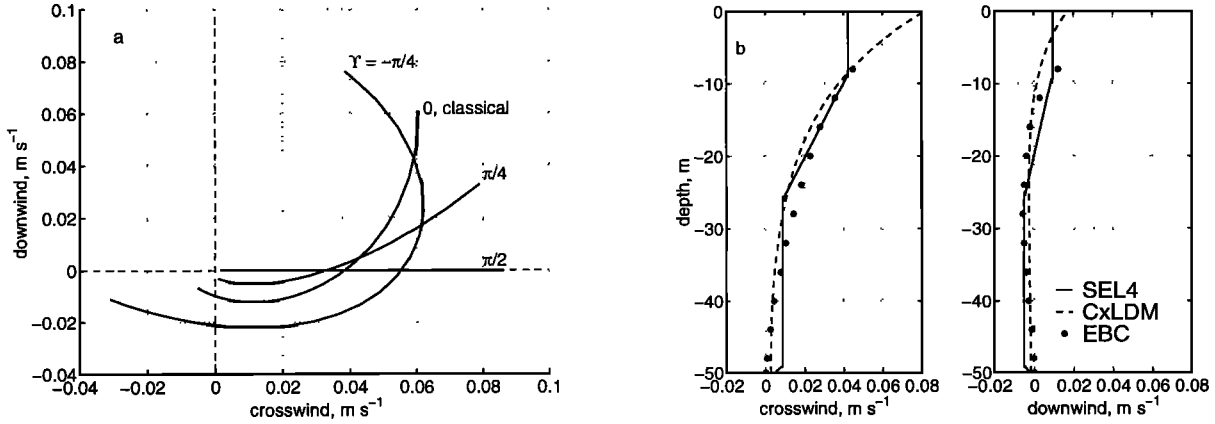


**Figure 18.** Solutions of the  $C_XLDM$  with external parameters set to EBC values. (a) Solutions for various  $\gamma$ . A classical spiral has  $\gamma = 0$  and stress parallel to shear, while  $\gamma > 0$  gives a stress to the left of the shear and flatter spirals. (b) Ekman layer currents computed by the SEL4 and  $C_XLDM$  solutions. The two solutions are generally similar, except in the upper 5 m of the water column, where the crosswind component of  $C_XLDM$  is considerably larger.

depth. However, solutions from models that included a depth-dependent diffusivity,  $K \propto 1 + z'$ , were not sufficiently different from the present laminar solutions to justify the complication of a depth-dependent  $K$  (Figure 4 is a partial but typical example).

The parameter dependence of this solution follows that of SEL2 and need not be examined in great detail. We do note three things. First, the  $C_XLDM$  solutions will be valid only in the fair weather regime defined in section 5.4.1. Second, in the large  $\alpha$  limit the surface current takes a particularly simple form,

$$V(0) = \frac{\sqrt{Q_* \pi \Omega^{-1}}}{f P_\tau} \exp[i(\pi/4 - \text{atan}(\frac{\Psi_i}{\Psi_r})/2)] \quad (26)$$

that may be compared with the CLDM surface current (12) and the SEL2 surface current (24). In this limit the speed of the  $C_XLDM$  surface current is independent of the stress, as in SEL2, but larger by a factor  $\sqrt{2}$  (Figure 17b). Third, the effect of solar heating can be assessed by factoring the diffusivity magnitude into terms that are familiar from planetary boundary layer theory,

$$K \approx \frac{U_*^2}{f} \frac{L}{U_*/f} \frac{\pi}{2} \sin(\phi),$$

or

$$K \approx U_* L \frac{\pi}{2} \sin(\phi),$$

where  $L = U_*^3/Q_* \approx 1.5$  m has the form of a Monin-Obukhov depth (taken positive for  $Q_*$  positive). The scale depth  $U_*/f \approx 100$  m, and thus the second term is roughly 0.015 (this is the equivalent of the similarity constant  $c_2$  of section 3.2). In this limit the diffusivity increases in direct proportion to the friction velocity times a Monin-Obukhov depth.

The  $C_XLDM$  diffusivity is given in terms of known, external variables and can be evaluated unambiguously.

The EBC and LOTUS3 cases are both within the large  $\alpha$  limit, and the diffusivity magnitudes from (25) are 80 and  $135 \times 10^{-4} \text{ m}^2 \text{ s}^{-1}$  for LOTUS3 and EBC, respectively. These are a little less than the diffusivity inferred from the CLDM fit to the data (Table 2) (recall that the CLDM fit was to the vector current and is thus a compromise between the speed (smaller  $K$ ) and the direction (larger  $K$ )). The angle  $\gamma$  is  $\sim 65^\circ$ , which is somewhat larger than inferred from the observations,  $\sim 45^\circ$ . This complex  $K$  and the solution (7) give a reasonable repeat of the SEL4 solution (Figure 18b), which was intended. There are differences in detail, especially very near the surface where there are no observations to discriminate between the two solutions. The  $C_XLDM$  solutions make good simulations of the midlatitude observations; for the LOTUS3 case the rms vector error =  $0.004 \text{ m s}^{-1}$  and PV = 98%, while for the EBC case the rms vector error =  $0.005 \text{ m s}^{-1}$  and PV = 94%. These are somewhat better than the optimum CLDM (Table 2) and without parameter adjustment. Thus for practical purposes the  $C_XLDM$  is a substantial improvement over the parameterized CLDM.

At tropical latitudes the simplified, large  $\alpha$  form fails as  $H$  becomes relevant. In that case the full SEL2 solution may be used to derive a depth scale that accounts for the current speed in the upper and lower layers, namely,  $D_K = [D_Q S_1 + (H - D_Q) S_2]/S_1$ . This gives  $K = 470 \times 10^4 \text{ m}^2 \text{ s}^{-1}$  and a reasonable simulation of the  $10^\circ \text{N}$  observations; rms vector error =  $0.016 \text{ m s}^{-1}$  and PV = 80% (or with the reduced stress, rms vector error =  $0.012 \text{ m s}^{-1}$  and PV = 90%). As before, the largest error is that the transition layer at the base of the Ekman layer is much too abrupt.

The  $C_XLDM$  solutions are as accurate as are the SEL4 solutions, and they have the considerable advantage of being continuous with depth. It would be straightforward to patch the fair weather  $C_XLDM$  form



onto a neutral form to arrive at a more complete Ekman layer model. The  $C_X$ LDM may thus be useful as a computational device in applications where a diffusion formulation is especially desirable. Even if the  $C_X$ LDM can serve to predict the fair weather Ekman layer, it surely does not explain it in any meaningful way. The complex diffusivity is formal rather than physical, and the rotation of the stress away from the shear arises upon time averaging a narrowband process (diurnal cycling) rather than from physical properties of upper ocean turbulence.

## 7. Depth of Semipermanent Stratification

To this point, all of the models have taken the depth of semipermanent stratification to be a given constant  $H$ . The actual depth of semipermanent stratification in the ocean varies significantly and on a wide range of timescales. In the LOTUS3 case, there were fast timescale variations of  $H$  due to internal wave motions (isotherm displacements at a depth of 50 m were about 4 m, rms; see Figure 10 [see also *Davis et al.*, 1981a, b]). There were significant variations associated with mesoscale weather (the high winds on day 168 caused the nighttime mixed layer to deepen from  $\sim 15$  to  $\sim 25$ –30 m), and it is well known that there are very large seasonal variations at most middle and high-latitude sites. These temporal variations of  $H$  are outside the scope of an Ekman layer model that is driven by time-averaged surface fluxes (mesoscale weather and seasonal variations can be treated by most numerical upper ocean models that can be driven by a time series of surface fluxes [*Large*, 1998]).

The consequences of the  $H$  variation can nevertheless be accounted for by a straightforward extension of the present model, provided that the amplitude is known and that the variation is either randomly or slowly (compared to  $f$ ) varying. In that event the effect of  $H$  variation is to cause a smearing over depth around the mean  $H$  without inducing significant turning (compare to the narrowband variability associated with diurnal cycling). Thus in the LOTUS3 case it would be plausible, if entirely ad hoc, to set the thickness of the lower interface (layer 4 in SEL4) to  $4 \times$  rms  $H' = 16$  m to represent the effect of random internal wave advection. This is much greater than the layer 4 thickness of SEL4 computed from a Richardson number condition and would give a more realistic solution at depth.

The effects of  $H$  variation are likely to be much more important at tropical latitudes where the deep Ekman layer currents are substantial. Indeed, almost all of the flatness in the  $10^\circ\text{N}$  profile arises from the unidirectional decay of the current between depths of  $\sim 40$  and 80 m, a feature not reproduced by any of the models. *Wijffels et al.* [1994] noted that the depth to the top of the thermocline was observed to vary from  $\sim 50$  to more than 100 m (probably mixed space and time variabil-

ity). Assuming that this  $H$  variation was either randomly or slowly varying, then its consequences can be evaluated roughly by computing the ensemble-averaged current profile for  $10^\circ\text{N}$  conditions with  $H$  varying from 50 to 100 m (Figure 17b). This can be compared to the solution for the average  $H$ , 75 m. The ensemble-averaged current decays smoothly and without turning over the depth range 50 to 100 m, while the solution for the average  $H$  necessarily shows an abrupt jump across  $z = -75$  m. The ensemble-averaged current profile is considerably more realistic than is the nominal solution having a fixed  $H$ , and the statistics are rms error =  $0.013 \text{ m s}^{-1}$  and PV = 86% or somewhat better than before (Table 2). This imposition of  $H$  variability would benefit the CLDM or any local model. It is interesting to consider that a lower interface layer can simply be added onto the profiles of SEL4 and  $C_X$ LDM since they were closed independently of these data. The CLDM, however, was fit to the data on the implicit assumption that a single (diffusive) length scale was appropriate for the entire Ekman layer. To the extent that the lower interface layer is the product of nonlocal  $H$  variability, then that was misguided and could result in a nonsensical estimate of  $K_b$ . To check whether this might have happened, we recomputed the fit to  $10^\circ\text{N}$  data of a modified CLDM having a 50-m-thick interface layer and recovered  $K_b = 600 \times 10^{-4} \text{ m}^2 \text{ s}^{-1}$  (but very poorly defined toward larger values). The misfit =  $0.013 \text{ m s}^{-1}$  and PV = 87% or much better than the straight CLDM. Thus we would still infer that  $K_b$  was somewhat larger than in the subtropics, though we are less sure of how much. A similarly modified null model does almost well, rms error =  $0.016 \text{ m s}^{-1}$  and PV = 83%.

This succession of models and fits to the  $10^\circ\text{N}$  data suggests the following characterization of the  $10^\circ\text{N}$  Ekman layer: The most important feature of the Ekman layer is the depth-averaged current, followed by the thick lower interface layer, and followed third by the diurnal-cycle-related shear of the upper Ekman layer (recall though that the upper 20 m was not sampled). In the subtropical cases the order is reversed; nearly all of the Ekman layer structure can be attributed to the diurnal-cycle-related shear of the upper Ekman layer, with the other features being relatively insignificant.

To the extent that  $H$  variability is nonlocal in origin, then the Ekman layer structure is not the product of the local surface fluxes alone, as we had assumed, conventionally, at the outset. To the growing list of relevant external variables should be added the rms  $H'$  or some equivalent measure of  $H$  variability.

## 8. Conclusions

### 8.1. Summary

**8.1.1. Question 1: What is the structure of the fair weather Ekman layer?** The current profile observed under fair weather conditions has a spiral shape in which the speed decays and the current vector

turns clockwise with increasing depth. This structure is similar to that of a classical Ekman spiral but differs in that the flatness is about 2–4 versus 1 or less for a classical spiral. In subtropical latitudes the Ekman layer was strongly surface trapped (speed  $e$ -folding in  $\sim 10$ – $15$  m), while at tropical latitudes the Ekman transport under similar wind stress and heat flux was distributed over a relatively thick layer ( $e$ -folding in  $\sim 30$  m), extending down to the top of the main thermocline.

**8.1.2. Question 2: Does the classical diffusion theory lead to a useful model of the fair weather Ekman layer?** The three fair weather cases considered here can be reproduced with some fidelity by the simplest classical laminar diffusion model or CLDM. The inferred diffusivity has an  $f$  and  $U_*$  dependence that is reminiscent of neutral, turbulent Ekman layer scaling but with a similarity constant reduced by a factor of  $\sim 3$  from its nominal, neutral value. It would be hard to find a simpler, more concise model than the parameterized CLDM, but there are problems in the details. The similarity constant has a significant parameter dependence, and classical diffusion models generally cannot reproduce the flatness seen in the observed profiles, evidently because the mean stress and the mean shear are not parallel. The upper ocean diffusivity appears to be as complicated as the current profile itself, and with hindsight it appears that the inductive diagnostic program was on a difficult path.

If the upper ocean diffusivity can be regarded as a formal rather than a physical quantity, then diffusion theory can be extended to allow a complex diffusivity, which is evidently required by the observations. A laminar form of a complex diffusivity was developed in section 6 based upon the results of a layered Ekman layer model. The resulting complex diffusion model,  $C_X$ LDM, can reproduce the phenomenon of the fair weather Ekman layer but is rather distant from a physical explanation.

**8.1.3. Question 3: What physical processes have to be represented in a minimum, realistic model of the fair weather Ekman layer?** This analysis has pursued the hypothesis that time-varying stratification is crucially important in the Ekman layer. Under fair weather conditions and outside of tropical latitudes, the structure of the Ekman layer appears to be determined, in large part, by the process of diurnal cycling. The thickness of the Ekman layer is proportional to the thickness of the diurnal warmed layer, and the flat spiral shape appears to be a result of the time-dependent stratification and mixing. It seems appropriate to call the resulting current spirals “stratified Ekman spirals.” The diurnal cycling process can be represented within either a time-dependent diffusion model or within a layered model. Either way, a realistic, flattened spiral emerges upon time averaging the solution. Because the shear within the density mixed layer is generally small compared to the shear overall in the Ekman layer, it is plausible to use a layered model

and develop an explicit solution, SEL2, that is dependent only upon external parameters (the addition of the third and fourth layers to make SEL4 was clearly ad hoc). The SEL4 solution is as accurate as the best fit CLDM.

While diurnal cycling often dominates stratification variability in the upper 10–20 m of the water column, other processes, e.g., internal wave advection and seasonality, will usually be more important at the greater depth of semipermanent stratification  $H$ . The error that results from ignoring this latter variability can be significant, especially in the tropics, where Ekman layer currents are substantial at depths well below the diurnal warm layer. If the  $H$  variability is known, then its effect on the Ekman layer can be evaluated approximately by forming an ensemble-averaged solution.

**8.1.4. Question 4: How does the Ekman layer structure vary with wind stress, latitude, and other external variables?** The three observed cases considered here are sufficient to demonstrate the dependence upon latitude only, and they show that the effect of decreased latitude is greater Ekman transport, as would have been expected, and a thicker Ekman layer. The SEL2 solution shows explicit dependence upon wind stress and heat flux; increased positive heat flux (or reduced wind stress) causes a reduced Ekman layer thickness. In the limit that the Ekman layer thickness is much less than the depth of semipermanent stratification, as commonly occurs at midlatitudes in summer, the (near) surface Ekman layer current of the SEL2 solution has a speed that is proportional to the square root of the midday heat flux and independent of the wind stress. In the tropics the effects of diurnal cycling are in some ways overwhelmed by the depth-averaged Ekman layer current, and the depth of semipermanent stratification and its variability become especially important.

Assuming that the most basic model of the Ekman layer would include as external variables  $U_*$ ,  $f$ ,  $z$ , and  $H$ , then to this we have added the daily maximum surface heat flux  $Q_*$ , the diurnal frequency  $\Omega$ , and a measure of the  $H$  variability, the rms  $H'$ . There is no sharp cutoff of this list; a complete or more precise account should include optical properties, if solar heating is important, and very likely some measure of surface wave properties, e.g., the Stokes drift [McWilliams *et al.*, 1997].

## 8.2. Closing Remarks

**8.2.1. Ekman layer models and observations.** This analysis has emphasized what are, on balance, small differences between models that from a distance would appear almost equally adequate to the data (Figure 5). Partly, this stems from the necessity of showing only the successful model solutions (e.g., the best fit CLDM solutions) but, more fundamentally, because the phenomenon we set out to understand and predict, the flattened fair weather Ekman spiral, is not diverse

or extensive. The result is that Ekman layer models are significantly underdetermined by the available historical observations. Additional current measurements made under less than fair weather conditions would help distinguish models, of course, as would measurements made very near the sea surface (Figure 17).

**8.2.2. Where is the turbulence?** In the opening remarks of section 1 we emphasized that a theory of the Ekman layer must be built around a model of turbulent transfer. The new Ekman layer solution SEL2 (or 4) developed in section 5 carries none of the usual earmarks, i.e., diffusivity or similarity constants, which might give the impression of a derivation from fundamentals. However, there were three important, empirical, and contingent properties of turbulent mixing embedded during the development of the SEL2 model. (1) Solar heating is sufficient to restratify the upper ocean in typical fair weather conditions, hence the importance of the diurnal cycle. (2) Vertical shear within the density mixed layer is small compared to the shear in the stratified diurnal jet, hence the use of a layered model. (3) The thickness of the diurnal warm layer is presumed set by a Richardson number condition, and hence  $D_Q$  relates wind stress and heat flux to warm layer thickness. Thus only a few simple results were needed to build a model of the mean current, but there are very important properties of the turbulence itself, for example, the rate of turbulent dispersion and the effects of large-scale turbulence upon Lagrangian trajectories, which this model and analysis were not able to address [McWilliams et al., 1997; Craig and Banner, 1994].

**8.2.3 In what sense is the stratified Ekman spiral real?** One difference between a stratified Ekman spiral and the classical Ekman spiral is that we expect that the former exists only on time average, i.e., only as a result of data (or model) analysis (Figure 9). In contrast, the classical Ekman spiral might have been presumed to exist, given the mere absence of temporal variability in the wind. That being so, then it would be interesting to examine the hydrodynamic stability of the classical spiral [Brown, 1991]. It may be less useful to do the same for the stratified Ekman spiral since no actual current profile is likely to bear more than a chance resemblance to the time-averaged profile. We noted in section 6 that the classical (steady) diffusivity appropriate to fair weather cases may be more a formal or theoretical than a physical quantity. The same could be said of the stratified Ekman spiral, at least insofar as fast timescale processes are concerned, e.g., the stirring process usually imagined to be represented by an eddy diffusivity.

**Acknowledgments.** The models discussed here are available from an anonymous ftp site, 128.128.29.54, pub/ekman, or directly from jprice@whoi.edu. J.F.P.'s research on upper ocean dynamics has been supported by the U.S. Office of Naval Research under grant N00014-95-1-0105.

Additional salary support during the time of manuscript preparation came from the National Science Foundation under grant OCE94-01300. M.A.S. was supported by the National Science Foundation under grant OCE90-05738. Our thanks to Peter Niiler, Bob Weller, and Al Plueddemann for stimulating discussions over many years and to Tony Sturges and Miles McPhee for their insightful critiques of an early draft. Mary Ann Lucas and Barbara Gaffron are thanked for their help with manuscript preparation. A preliminary report of this research was presented at the 1998 NATO Workshop on Ocean Modeling and Parameterization held in Les Houches, France, and summarized by Price [1998].

## References

- Anis, A., and J. N. Moum, Surface wave-turbulence interactions: Scaling  $\epsilon(z)$  near the sea surface, *J. Phys. Oceanogr.*, **25**, 2025–2045, 1995.
- Brainerd, K. E., and M. C. Gregg, Diurnal restratification and turbulence in the oceanic surface mixed layer, 1, Observations, *J. Geophys. Res.*, **98**, 22,645–22,656, 1993a.
- Brainerd, K. E., and M. C. Gregg, Diurnal restratification and turbulence in the oceanic surface mixed layer, 2, Modeling, *J. Geophys. Res.*, **98**, 22,657–22,664, 1993b.
- Briscoe, M. G., and R. A. Weller, Preliminary results from the Long-Term Upper Ocean Study (LOTUS), *Dyn. Atmos. Oceans*, **8**, 243–265, 1984.
- Brown, R. A., *Fluid Mechanics of the Atmosphere*. Academic, San Diego, Calif., 1991.
- Chereskin, T. K., Direct evidence for an Ekman balance in the California Current, *J. Geophys. Res.*, **100**, 18,261–18,269, 1995.
- Chereskin, T. K., W. D. Wilson, H. L. Bryden, A. Field, and J. Morrison, Observations of the Ekman balance at 8°30'N in the Arabian Sea during the 1995 southwest monsoon, *Geophys. Res. Lett.* **24**, 2541–2544, 1997.
- Coleman, G. N., J. H. Ferziger, and P. R. Spalart, A numerical study of the turbulent Ekman layer, *J. Fluid Mech.*, **213**, 313–348, 1990.
- Craig, P. D., and M. L. Banner, Modeling wave-enhanced turbulence in the ocean surface layer, *J. Phys. Oceanogr.*, **24**, 2546–2559, 1994.
- D'Asaro, E. A., and G. T. Dairiki, Turbulence intensity measurements in a wind-driven mixed layer, *J. Phys. Oceanogr.*, **27**, 2009–2022, 1997.
- D'Asaro, E. A., D. M. Farmer, and G. T. Dairiki, A Lagrangian float, *J. Atmos. Oceanic Technol.*, **13**, 1230–1246, 1996.
- Davis, R. E., R. DeSzoeko, D. Halpern, and P. Niiler, Variability in the upper ocean during MILE, I, The heat and momentum balances, *Deep Sea Res., Part A*, **28**, 1427–1451, 1981a.
- Davis, R. E., R. DeSzoeko, and P. Niiler, Variability in the upper ocean during MILE, II, Modeling the mixed layer response, *Deep Sea Res., Part A*, **28**, 1453–1475, 1981b.
- Ekman, V. W., On the influence of the earth's rotation on ocean currents, *Arch. Math. Astron. Phys.*, **2**, 1–52, 1905.
- Frisch, U., *Turbulence*. Cambridge Univ. Press, New York, 1995.
- Gnanadesikan, A., and R. A. Weller, Structure and instability of the Ekman spiral in the presence of surface gravity waves, *J. Phys. Oceanogr.*, **25**, 3148–3171, 1995.
- Huang, N. E., On surface drift currents in the ocean, *J. Fluid Mech.*, **91**, 191–208, 1979.
- Karniadakis, G. E., and G. L. Brown, Vorticity transport in

- modeling three-dimensional unsteady shear flows, *Phys. Fluids*, **7**, 688–690, 1995.
- Krauss, W., Ekman drift in homogeneous waters, *J. Geophys. Res.*, **98**, 20,187–20,209, 1993.
- Krauss, W., On the slippage of deep-drogued drifters, *J. Geophys. Res.*, **101**, 1309–1319, 1996.
- Large, W. G., Modeling and parameterizing the ocean planetary boundary layer, in *Ocean Modelling and Parameterization*, edited by E. P. Chassignet and J. Verron, pp. 81–120, Kluwer Acad., Norwell, Mass., 1998.
- Large, W. G., and S. Pond, Open ocean momentum flux measurements in moderate to strong winds, *J. Phys. Oceanogr.*, **11**, 324–326, 1981.
- Large, W. G., J. C. McWilliams, and S. C. Doney, Oceanic vertical mixing: A review and a model with nonlocal boundary layer parameterization, *Rev. Geophys.*, **32**, 363–403, 1994.
- Lee, C. M., and C. C. Eriksen, The subinertial momentum balance of the North Atlantic subtropical convergence zone, *J. Phys. Oceanogr.*, **26**, 1690–1704, 1996.
- Levitus, S., Climatological atlas of the world ocean, *NOAA Prof. Pap. 13*, U.S. Govt. Print. Office, Washington, D.C., 1982.
- Madsen, O. S., A realistic model of the wind-induced Ekman boundary layer, *J. Phys. Oceanogr.*, **7**, 248–255, 1977.
- McPhee, M.G., Small-scale processes, in *Polar Oceanography Part A, Physical Science*, chap. 6, pp. 287–334, Academic, San Diego, California, 1990.
- McPhee, M. G., and D. G. Martinson, Turbulent mixing under drifting pack ice in the Weddell Sea, *Science*, **263**, 218–221, 1994.
- McWilliams, J. C., P. S. Sullivan, and C.-H. Moeng, Langmuir turbulence in the ocean, *J. Fluid Mech.*, **334**, 1–30, 1997.
- Mellor, G. L., and P. A. Durbin, The structure and dynamics of the ocean surface mixed layer, *J. Phys. Oceanogr.*, **5**, 718–728, 1975.
- Neumann, G., and W. J. Pierson, *Principles of Physical Oceanography*, 545 pp., Prentice-Hall, Engelwood Cliffs, N.J., 1966.
- Niiler, P. P., and J. Paduan, Wind-driven motions in the northeast Pacific as measured by Lagrangian drifters, *J. Phys. Oceanogr.*, **25**, 2819–2830, 1995.
- Peixoto, J. P., and A. H. Oort, *Physics of Climate*, Am. Inst. of Phys., New York, 1992.
- Pollard, R. T., Observations and models of the structure of the upper ocean, in *Modelling and Prediction of the Upper Layers of the Ocean*, edited by E. B. Kraus, pp. 102–117, Pergamon, Tarrytown, N.Y., 1975.
- Price, J. F., Parameterization of the fair weather Ekman layer, in *Ocean Modelling and Parameterization*, edited by E. P. Chassignet and J. Verron, pp. 121–134, Kluwer Acad., Norwell, Mass., 1998.
- Price, J. F., R. A. Weller, and R. Pinkel, Diurnal cycling: Observations and models of the upper ocean response to heating, cooling, and wind mixing, *J. Geophys. Res.*, **91**, 8411–8427, 1986.
- Price, J. F., R. A. Weller, and R. R. Schudlich, Wind-driven ocean currents and Ekman transport, *Science*, **238**, 1534–1538, 1987.
- Rossby, C.-G., and R. B. Montgomery, The layer of frictional influence in wind and ocean currents, *Pap. Meteorol. Oceanogr.*, **3**(3), 1935.
- Schudlich, R. R., and J. F. Price, Observations of the seasonal variation in the Ekman layer, *J. Phys. Oceanogr.*, **28**, 1187–1204, 1998.
- Stacey, M. W., S. Pond, and P. H. LeBlond, A wind-forced Ekman spiral as a good statistical fit to low-frequency currents in a coastal strait, *Science*, **233**, 470–472, 1986.
- Stommel, H., K. Saunders, W. Simmons, and J. Cooper, Observations of the diurnal thermocline, *Deep Sea Res.*, **16**, 269–284, 1969.
- Weller, R. A., Observations of the velocity response to wind forcing in the upper ocean, *J. Geophys. Res.*, **86**, 1969–1977, 1981.
- Weller, R. A., and R. E. Davis, A vector measuring current meter, *Deep Sea Res., Part A*, **27**, 565–582, 1980.
- Weller, R. A., and A. J. Plueddemann, Observations of the vertical structure of the oceanic boundary layer, *J. Geophys. Res.*, **101**, 8789–8806, 1996.
- Weller, R. A., and J. F. Price, Langmuir circulation within the oceanic mixed layer, *Deep Sea Res., Part A*, **35**, 711–747, 1988.
- Wijffels, S., E. Firing, and H. Bryden, Direct observations of the Ekman balance at 10N in the Pacific, *J. Phys. Oceanogr.*, **24**, 1666–1679, 1994.
- Yu, L., and J. J. O'Brien, Variational estimation of the wind stress drag coefficient and the oceanic eddy viscosity profile, *J. Phys. Oceanogr.*, **21**, 709–719, 1991.

---

J. F. Price, Physical Oceanography Department, Mail Stop 29, Woods Hole Oceanographic Institution, Woods Hole, MA 02543. (jprice@whoi.edu)

M. A. Sundermeyer, Center for Marine Science and Technology, University of Massachusetts, New Bedford, MA 02748.

(Received May 17, 1996; revised May 13, 1999; accepted May 19, 1999.)